Shortwave Radiative Impacts of the Asian Tropopause Aerosol Layer (ATAL) using Balloon-borne In-situ measurements at three distinct locations in India

Vadassery Neelamana Santhosh[1~~,2~~], Bomidi Lakshmi Madhavan[1], Sivan Thankamani Akhil Raj[2], Madineni Venkat Ratnam[1], Jean-Paul Vernier[3,4], and Frank Gunther Wienhold[5]

[1]National Atmospheric Research Laboratory (NARL), Gadanki 517 112, India
[2]India Meteorological Department (IMD), New Delhi 110 003, India
[3]National Institute of Aerospace, Hampton, VA, USA
[4]NASA Langley Research Center, USA
[5]Institute of Atmospheric and Climate Science (IAC), ETH, Zurich, Switzerland

Correspondence to:
Bomidi Lakshmi Madhavan (~~madhavanbomidi@gmail.com~~madhavanbomidi@gmail.com, ~~blmadhavan@narl.gov.in~~blmadhavan@narl.gov.in)

Abstract

~~The recurring presence~~This study aims to investigate the direct shortwave radiative forcing and heating rates of the Asian Tropopause Aerosol Layer (ATAL) in the Upper Troposphere Lower Stratosphere (UTLS) region~~, strongly linked with the Asian Summer Monsoon Anticyclone (ASMA), has garnered significant attention over the past decade. However, despite advances in instrumentation, studies quantifying the radiative impacts of ATAL aerosols in terms of radiative forcing and heating rates remain limited. This study aims to address this gap by evaluating the direct radiative effects of ATAL aerosols in the UTLS~~ using in-situ ~~measurements~~observations from the Balloon measurement campaigns of the Asian Tropopause Aerosol Layer (BATAL) ~~campaigns ~~conducted between 2014 and ~~2019~~2018. Measurements were obtained over three distinct locations in India: Gadanki (13.48°N, 79.18°E), Hyderabad (17.47°N, 78.58°E), and

Varanasi (25.27°N, 82.99°E). ~~The study considers three scenarios where UTLS aerosols are predominantly composed of sulfates, nitrates, or anthropogenic aerosols. Our findings reveal significant changes in aerosol radiative forcing, ranging from -0.015 to 0.03 Wm^{-2} at the top of the atmosphere, -0.01 Wm^{-2} to -0.16 Wm^{-2} at the surface, and 0 to 0.19 Wm^{-2} within the atmospheric column when transitioning from sulfate to nitrate and anthropogenic aerosol scenarios. UTLS aerosols were found to contribute 0.1% to 2.3% of the total columnar atmospheric forcing, with the highest contributions observed under the anthropogenic scenario. Notably, heating rate profiles indicate enhanced aerosol heating under anthropogenic scenarios, with rates reaching up to 0.03 K day^{-1}, particularly over Varanasi, compared to significantly lower rates under sulfate and nitrate scenarios. The study highlights the spatial variability in radiative impacts across different locations, reflecting the structural and dynamic complexities of ATAL within the ASMA region. It emphasizes the need for a comprehensive approach combining in-situ, satellite, and model-based retrievals to overcome current limitations and achieve a more accurate understanding of the net radiative impacts of ATAL aerosols.~~Given the ambiguity in the chemical composition of ATAL from several reported studies, seven different aerosol mixtures—comprising sulfate, nitrate, organic carbon, and ammonium—were considered to assess their impact on estimates of ATAL radiative forcing and heating rates. A pronounced enhancement in aerosol backscatter was observed at ATAL altitudes (13 to 19 km) across all locations, with the backscatter ratio (at 455 nm) peaking at 1.07 over Varanasi and Hyderabad, followed by 1.06 over Gadanki. Radiative forcing estimates indicate a net warming effect, with ATAL contributing up to 3% of the total columnar atmospheric forcing. Heating rates reveal a marked increase in aerosol-induced warming at ATAL altitudes, with maximum heating rates reaching 0.03 K day^{-1} across the study locations. The radiative impact of ATAL aerosols is highly sensitive to variations in the aerosol composition.

Compared to a reference case with a stratospheric sulfate background, the ATAL radiative forcing varies between 0.03 and 0.28 W m^{-2} (1.5 to 14-fold increase). At the same time, heating rates exhibit a 30-fold increase, reaching 0.03 K day^{-1}, depending on the aerosol mixture. Despite these strong localized effects within the UTLS, the overall contribution to total columnar aerosol forcing remains moderate (up to 5%), underscoring the importance of aerosol composition in determining ATAL's radiative influence.

Keywords: *Asian Tropopause Aerosol Layer; Aerosol-Radiation Interaction; Radiative forcing and heating rates; Upper Troposphere-Lower Stratosphere*

1. ~~1.~~ Introduction

The Asian summer monsoon~~ (~~, which occurs from June~~-~~ to August~~) over the northern hemisphere is known for~~, plays a crucial role in transporting pollutant-laden air masses ~~over~~across a vast geographic region~~.~~ in the Northern Hemisphere (e.g., Vogel et al., 2024; Yu et al., 2017). A large-scale anti-cyclonic circulation, known as the Asian Summer Monsoon Anticyclone (ASMA), ~~forms~~develops in the Upper Troposphere Lower Stratosphere (UTLS) due to intense heating over the Tibetan ~~plateau~~Plateau, coupled with ~~persistent~~ deep convection over the head Bay of Bengal (BoB). This system effectively traps and ~~isolates~~redistributes air masses~~, dispersing them across~~ within a broad ~~geographic area (10°~~ region (10°N~~ to 40°~~–40°N~~ and 10°~~, 10°E~~ to 140°~~–140°E) (~~e.g.~~von Hobe et al., 2021; Lelieveld et al., 2018; Park et al., 2007; Randel and Park, 2006), leading to ~~persistent extremes of~~significant enhancements in trace constituents such as water vapor, methane, nitrogen dioxide, ozone~~, etc.~~ around the ASMA center (~~e.g.~~ Basha et al., 2021; Kumar and Ratnam, 2021; Park et al., 2007). Satellite observations have ~~also revealed~~identified a ~~recurrent layer of~~persistent aerosol ~~enhancements~~enhancement in the UTLS (~ 13–18 km) during the monsoon, known as the Asian Tropopause Aerosol Layer (ATAL~~), in the UTLS region (~ 13-18~~

~~km), which significantly impacts stratospheric composition, chemistry, cirrus cloud characteristics, and the Earth's radiative balance~~) (Vernier et al., 2011~~;~~, 2015; Thomason and Vernier, 2013). The ATAL is of particular scientific interest due to its potential influence on stratospheric composition, chemistry, cirrus cloud properties, and the Earth's radiative balance.

The formation and dissipation of ATAL are closely linked to deep convection ~~during the monsoon~~, which transports aerosols from the ~~Bay of Bengal~~BoB and ~~the~~ surrounding land areas into the UTLS ~~region~~ (He et al., 2020). ~~Aerosols are non-homogeneously distributed within the~~However, ATAL~~, and descending motion in the western part of the ASMA region plays an important role in the dissipation of the layer. Fadnavis et al. (2013) demonstrated through simulations that the deep convection and the associated heat-driven circulation over the southern side of the Himalayas are the dominant transport pathway of~~ aerosols ~~into the UTLS together with notable anthropogenic contribution. Neely et al. (2014) further emphasized broader source regions for ATAL aerosols beyond solely Asian SO$_2$ emissions. Specifically,~~exhibit significant spatial and temporal variability, reflecting their ~~results showed that SO$_2$ emissions from China and India contributed ∼30% of the sulfate aerosol extinction in the ATAL during volcanically quiescent periods. Recent simulations using GEOS-Chem indicated that the contribution from India and China could double those estimates, with both countries contributing equally (30%)~~ diverse sources and transport pathways (Fairlie et al., 2020~~).~~; Lau et al~~. (~~., 2018~~) indicated two preferred pathways for the strong vertical transport of the carbonaceous and dust aerosols toward the ATAL region, one over the Himalaya-Gangetic Plain (India) and the other one over the Sichuan basin (China) located in the southern and eastern foothills of the Tibetan Plateau respectively. These different sources and pathways indicate the possible~~; Neely et al., 2014; Fadnavis et al., 2013). The presence of ~~wide ranges of~~ both natural and anthropogenic aerosols~~, which are further~~

~~influenced by the~~ within ATAL, combined with dynamic and chemical ~~processes,~~ interactions—including secondary aerosol formation~~, within the ASMA region as suggested by recent chemical analysis (~~—further complicates its characterization. Recent studies indicate that a substantial fraction of ATAL aerosols results from gas-to-particle conversion of inorganic and organic precursors, highlighting the role of secondary aerosol formation in this region (Appel et al., 2022).

~~There are varied opinions on the chemical composition of the ATAL region. Vernier et al. (2015) noted that the bottom part of the ATAL is dominated by the sulfate aerosols, with the carbon-to-sulfate ratio ranging from 2 to 10. Later, model simulations by Yu et al. (2015) revealed a dominant sulfate contribution together with surface-emitted and secondary organics. Fadnavis et al. (2013) also reported the presence of sulfate aerosols together with black carbon (BC), organic carbon (OC), and mineral dust. The significant lofting of mineral dust to the ATAL region was noted in the simulations by~~ Despite growing interest in ATAL, its optical and radiative properties remain poorly constrained due to limitations in observational datasets. Aerosol optical depth (AOD) and extinction coefficient measurements in the UTLS are hindered by low aerosol concentrations, instrumental detection thresholds, and retrieval uncertainties in satellite and lidar observations. Additionally, complex transport and mixing processes in the UTLS make it challenging to determine ATAL's chemical composition, which is critical for quantifying its optical properties—such as single scattering albedo (SSA) and asymmetry parameter (ASY)—that govern radiative transfer calculations. Early studies primarily identified sulfate as the dominant component of ATAL (e.g., Vernier et al., 2015; Yu et al., 2015; Fadnavis et al., 2013). However, subsequent investigations revealed a more diverse aerosol composition. A reanalysis study for the summer of 2008 detected significant contributions from mineral dust and carbonaceous aerosols transported by deep convection (Lau et al., 2018). Long-term simulations (2000–2015) using the

Community Earth System Model further indicated that ATAL aerosols comprise approximately 40% sulfate, 30% secondary aerosols, 15% primary aerosols, 14% ammonia-based aerosols, and trace amounts of black carbon (Bossolasco et al., 2021). Additionally, combined satellite, high-altitude aircraft, and cloud-chamber studies suggested the dominance of ammonium nitrate particles in the upper troposphere (Höpfner et al., 2019). Several in situ studies have also reported a substantial nitrate fraction in ATAL (e.g., Vernier et al., 2022; Vernier et al., 2018), with aircraft-based chemical analyses indicating significant contributions from particulate nitrate, ammonium, and organic aerosols at 13–18 km (Appel et al., 2022).

Understanding the radiative impacts of ATAL remains a major research challenge due to the uncertainties in aerosol composition, optical properties, and vertical distribution. Limited studies have quantified its radiative effects.~~Ma et al. (2019), and they further revealed that hygroscopic aerosols (such as nitrates and sulfates) and associated liquid water influence the extinction in the UTLS region. Lau et al. (2018) previously reported the presence of dust, carbonaceous aerosols, and carbon monoxide (CO), which are lofted through orographically forced deep convection into the ATAL region. Long-term simulations (2000 to 2015) by Bossolasco et al. (2021) indicated that aerosols other than mineral dust in the ATAL consist of ~ 40% sulfate, 30% secondary aerosols, 15% primary aerosols, 14% of ammonia-based aerosols, and less than 3% BC. GEOS-Chem simulation by Fairlie et al. (2020) further revealed a dominant contribution of nitrate aerosols at the southern side of the ASMA region. While the findings from model-based studies varied, many in-situ studies concur on the relative dominance of nitrate aerosols in the ATAL. The first-ever offline chemical analysis from the BATAL campaigns over India revealed that there exists a dominant nitrate contribution in the ATAL, and surprisingly, the sulfate aerosols were below the detection limit of the instrument (Vernier et al. 2018). Later, Vernier et al. (2022)~~

~~indicated the dominant presence of nitrate and nitrite aerosols with concentrations between 88 and 374 ng m^{-3} at STP during the 2017 BATAL campaign. Höpfner et al. (2019) demonstrated the dominant ammonium nitrate particles in the upper troposphere during the Asian monsoon period using satellite and high altitude aircraft measurements combined with atmospheric trajectory simulations and cloud chamber experiments. Appel et al. (2022) observed enhancements in the mass concentrations of particulate nitrate, ammonium, and organics in altitudes between ~ 13 and 18 km using airborne instruments. Their aerosol mass spectrometry analysis further revealed that the particles in the ATAL mainly consist of ammonium nitrate (AN) and organics.~~

~~Owing to the complexity of retrieving the aerosol properties required for the radiative impact estimations, the studies on ATAL radiative forcing and heating rates are sparse.~~ Vernier et al. ~~Vernier et al.~~ (2015) ~~used long-term satellite measurements to determine that the~~reported an increase in summertime ~~aerosol optical depth~~AOD over Asia~~,~~ associated with ~~the~~ ATAL~~, increased~~ from 0.002 to 0.006 between 1995 and 2013~~. This increase resulted in~~ , leading to a ~~short-term~~ regional shortwave radiative forcing of -0.12 W m^{-2} at the top of the atmosphere ~~of −0.01 Wm^{-2}, compensating for about one-third of the radiative~~ (TOA). This forcing ~~associated with the~~ partially offset (~33%) the radiative impact of global ~~increase in~~ CO~~$_2$. They also noted that the regional radiative forcing caused by the ATAL varies between clear-sky and all-sky conditions. Under all-sky conditions, calculations showed lesser shortwave radiative forcing over the monsoon region due to cloudiness. Using simulations with~~ $_2$ increases during 2000–2010 (Solomon et al., 2011). Using MERRA-2 reanalysis~~ data~~, Gao et al. (2023) ~~demonstrated that ATAL impacts clear-sky shortwave fluxes at the TOA and surface. For the time-averaged ATAL relative to the no-aerosol case, the net effects include a~~ estimated that ATAL aerosols exert a clear-sky positive radiative forcing of 0.15 W m~~$^{-2}$ increase in incoming solar radiation at the TOA and a 0.72 W m^{-2} reduction~~

~~in absorbed shortwave radiation at the surface. Over the past decade, the radiative forcing due to ATAL led to a summertime reduction in surface temperature, although this effect has not yet been quantified.~~

~~Despite the recognized importance of ATAL in climate studies, research on its radiative forcing and heating rates from in-situ measurements is non-existent due to challenges in retrieving relevant aerosol~~ $^{-2}$ at 20 km due to their absorption properties. ~~The~~Chemistry-climate modeling by Fadnavis et al. (2022) further demonstrated that carbonaceous aerosols induce tropospheric and lower stratospheric heating of 0.02–0.3 K per month, thereby enhancing water vapor transport into the UTLS. Similarly, Chavan et al. (2021) showed that biomass-burning aerosols over Asia contribute to UTLS heating rates of 0.001–0.02 K day^{-1}.

Despite these insights, significant gaps remain in our understanding of ATAL's radiative effects. The contribution of ATAL aerosols to total atmospheric forcing is largely unknown, and real-time, high-resolution, altitudinal in-situ observations remain scarce. Moreover, previous estimates rely predominantly on reanalysis or model-based studies, which introduce uncertainties due to several assumptions. Therefore, there is a need for direct observational constraints on ATAL radiative forcing and heating rates.

To address these gaps, the Balloon measurement campaigns for the Asian Tropopause Aerosol Layer (BATAL) ~~consist of~~provide high-resolution in-situ measurements of aerosol and atmospheric properties~~ at three different locations over India.~~, offering a unique opportunity to refine radiative transfer calculations for ATAL. This study ~~aims~~leverages BATAL observations to ~~address several research aspects, including the extent of aerosol enhancement in the UTLS during the late monsoon, the radiative forcing~~(i) characterize ATAL enhancements across ~~different scenarios of UTLS aerosols,~~multiple BATAL study locations, (ii) quantify ATAL radiative forcing and heating rates within the UTLS (12-20 km) using the high-resolution in-situ measurements, (iii) assess the contribution of ATAL to total atmospheric column forcing, (iv) ascertain the sensitivity of ATAL radiative forcing and ~~the resulting~~ heating rates to variations in aerosol compositions, and (v) compare the heating rate ~~patterns.~~

~~In the following sections~~estimates from in-situ measurements from the three-point locations with spatially averaged estimated derived from satellite observations to ascertain their regional representativeness and variability. To achieve these objectives, we ~~provide~~ introduce a methodological framework that integrates in-situ data to screen clouds, identify potential aerosol types or compositions, and incorporate these observations into radiative transfer calculations.

The paper is structured as follows: Section 2 provides a brief description of the BATAL ~~campaigns~~ and study locations ~~(**Section 2**), describe the datasets used (~~, Section 3~~), and~~ details ~~of~~the datasets used, and Section 4 outlines the methodology for estimating radiative impacts ~~(**Section 4**)~~.. The results are discussed in Section 5, followed by ~~the listing~~a summary of key findings in Section 6.

2. ~~2.~~ Campaign Details and Observation Sites

~~The Balloon Measurement Campaigns of the Asian Tropopause Aerosol Layer (BATAL) was~~The BATAL campaigns were conducted jointly by the Indian Space Research Organization (ISRO) and the National Aeronautics and Space Administration (NASA) during the ~~last phase of the~~late monsoon season (July ~~to~~ –September) from 2014 to ~~2019~~2018. These campaigns ~~involved over a hundred balloon flights~~deployed high-altitude balloons equipped with miniature payloads to ~~study~~investigate the optical properties, size distribution, and composition of aerosols in the ATAL. ~~The BATAL also~~Additionally, the campaigns focused on ~~investigating~~ examining the behavior of ozone and water vapor ~~behavior~~ in the UTLS and assessing the ~~impact~~role of deep convection ~~over the ATAL~~in transporting aerosols and trace gases to this region. For ~~more~~ detailed ~~information on~~descriptions of the payloads, balloon ~~types~~specifications, and other scientific objectives, refer to Vernier et al. ~~(2018). These experiments were conducted in three distinct locations (in terms of the local weather and surface emissions) in India (**Fig. 1**):~~(2018).

The BATAL campaigns were conducted at three distinct sites in India, chosen based on their local weather, emission characteristics, and recovery of payload (**Fig. 1**):

(i) **Gadanki (13.48°N, 79.18°E**~~):~~**)** – A rural background location in southern peninsular India with hilly topography. ~~The site experiences surface emissions~~ Aerosol sources in this region are primarily from vehicular ~~sources~~emissions, agricultural activities, and wood burning. During the monsoon season, the site experiences surface ~~pressure ranges from~~pressures between 960 ~~to~~and 965 hPa, ~~with~~ temperatures ~~between~~ranging from 27°C ~~and~~to 30°C~~. The~~, and prevailing ~~south-westerly~~southwesterly winds ~~range from~~of 1.5 to 1.6 m~~/~~ s~~, and the~~$^{-1}$. The relative humidity is typically ~~less than 60%. The Aerosol Optical Depth (AOD) at 500 nm ranges from 0.4 to 0.5, dominated by~~ below 60%. Sky radiometer observations from this location revealed the presence of dominant coarse-mode aerosols during the monsoon (Santhosh et al., 2024a; Madhavan et al., 2021).

(ii) **Hyderabad (17.47°N, 78.58°E**~~):~~**)** – A rapidly urbanizing megacity ~~located~~situated on the Deccan Plateau. ~~It~~This region has a semi-arid climate~~, with~~ characterized by significant seasonal variations in temperature and humidity. ~~Local~~Anthropogenic sources primarily drive local emissions ~~are highly polluted, with~~, whereas long-range aerosol transport is more prevalent during ~~the monsoon. AOD measurements during~~ the monsoon season~~-~~. AOD measurements indicate ~~a dominant contribution from~~that coarse-mode aerosols contribute significantly to the overall aerosol burden (Ratnam et al., 2020; Sinha et al., ~~2012~~2013).

(iii) **Varanasi (25.27°N, 82.99°E**~~): –~~) – An urban ~~location~~site in the Indo-Gangetic Plain (IGP~~), experiencing~~) characterized by a humid subtropical climate with ~~significant~~pronounced seasonal variations in temperature and rainfall. The region ~~is highly polluted, with large variability in~~experiences high aerosol loading ~~observed throughout the year.~~due to a mix of natural and anthropogenic sources. Coarse-mode aerosols, primarily dust, dominate ~~during~~in the pre-monsoon months, while fine-mode anthropogenic aerosols, including carbonaceous and sulfate aerosols, are more ~~prevalent~~prominent during the post-monsoon and winter months (Murari et al., 2017; Tiwari and Singh, 2013).

~~3.~~

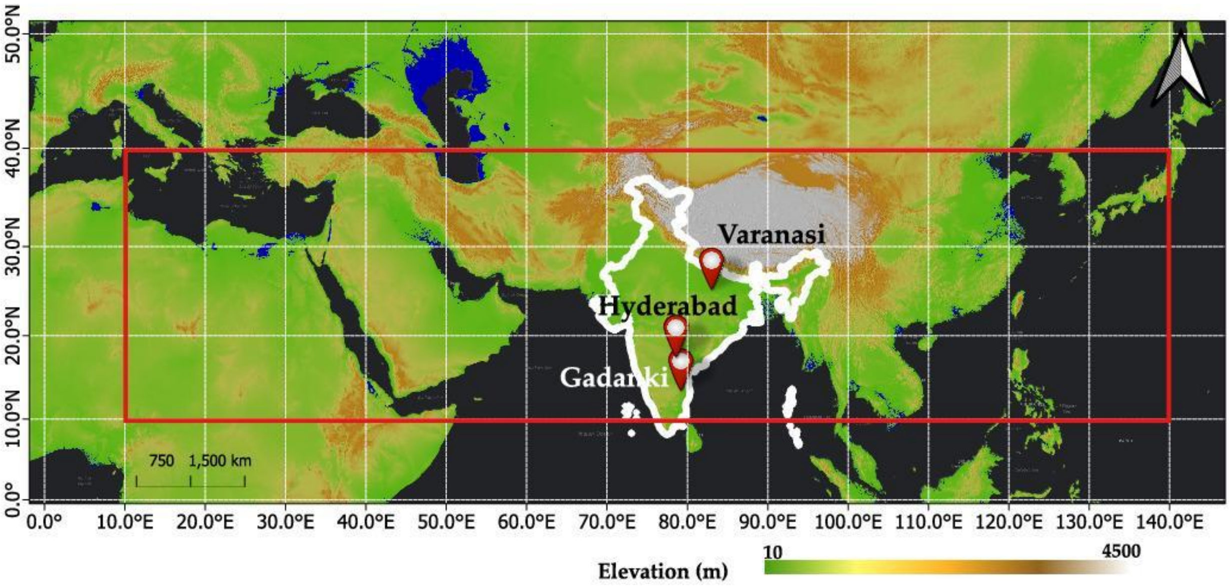

Figure 1: Balloon launch sites during the 2014-2018 BATAL campaigns. The red box outlines the typical geographic extent of the Asian Tropopause Aerosol Layer (ATAL) region, spanning 10°E–140°E and 10°N–40°N.

These strategically selected sites offer critical insights into the spatial variability of aerosols that influence the ATAL, enabling a comprehensive assessment of their chemical composition, transport pathways, and radiative impacts in the UTLS.

3. Datasets

~~We used data~~Among the multiple payloads launched during the BATAL campaigns, this study focuses on measurements from radiosondes~~,~~ and ozonesondes~~,~~ (for atmospheric parameters) and the Compact Optical Backscatter Aerosol Detector (COBALD) (for aerosol measurements).

3.1. Radiosonde and Ozonesonde

We utilized pressure, temperature, and relative humidity (RH) data from radiosondes, along with ozone volume mixing ratios from ozonesondes, to generate user-defined atmospheric profiles for the radiative forcing calculations. The Meisei (RS-11 G) and iMet radiosondes were used to measure temperature and pressure at different altitudes. The iMet radiosondes employed piezo-resistors for atmospheric pressure measurements, with an accuracy of 1–2 hPa. The Meisei radiosonde, which lacks a pressure sensor, derived pressure values from temperature and GPS altitude data. Ozone mixing ratios were obtained using EN-SCI Electrochemical Concentration Cell (ECC) ozonesondes, following the methodology outlined by Komhyr et al. (1995). More details on these methodologies can be found in Ratnam et al. (2014) and Akhil Raj et al. (2015).~~from the BATAL to derive the aerosol extinction and atmospheric~~ The observed atmospheric parameter profiles~~. In this study, we used~~ in the UTLS region are shown in **Figure S1.**

3.2. Compact Optical Backscatter Aerosol Detector (COBALD)

COBALD, developed by ETH Zurich, is a lightweight, balloon-borne sonde designed to measure backscattered light from aerosols, molecules, and clouds (Vernier et al., 2018). It operates with two LED light sources emitting at 455 nm (blue) and 940 nm (red) wavelengths. The emitted light illuminates the surrounding air, and a silicon photodetector captures the backscattered signal from particles within a 0.5-meter range. Approximately 90% of the measured backscattering signal originates from within a 10-meter radius of the instrument. COBALD operates without requiring external airflow and transmits real-time backscatter data, alongside pressure and temperature measurements, to the ground station at a frequency of 1 Hz. The instrument has an uncertainty of 5% and a precision better than 1% in the UTLS region (Vernier et al., 2015, 2018).

Details of the balloon launches from which the present study's measurements were obtained are summarized in **Table 1**. We considered those balloon-borne in-situ measurements~~ covering,~~ which covered a minimum altitude of 20 km~~. COBALD measurements after August 15, 2017, were excluded to avoid the possible influence of the Canadian wildfires and the Raikoke eruption (Akhil Raj et al., 2022). The details of the data used in this study are provided in **Table 1**.~~ above the surface, to capture the ATAL signal effectively.

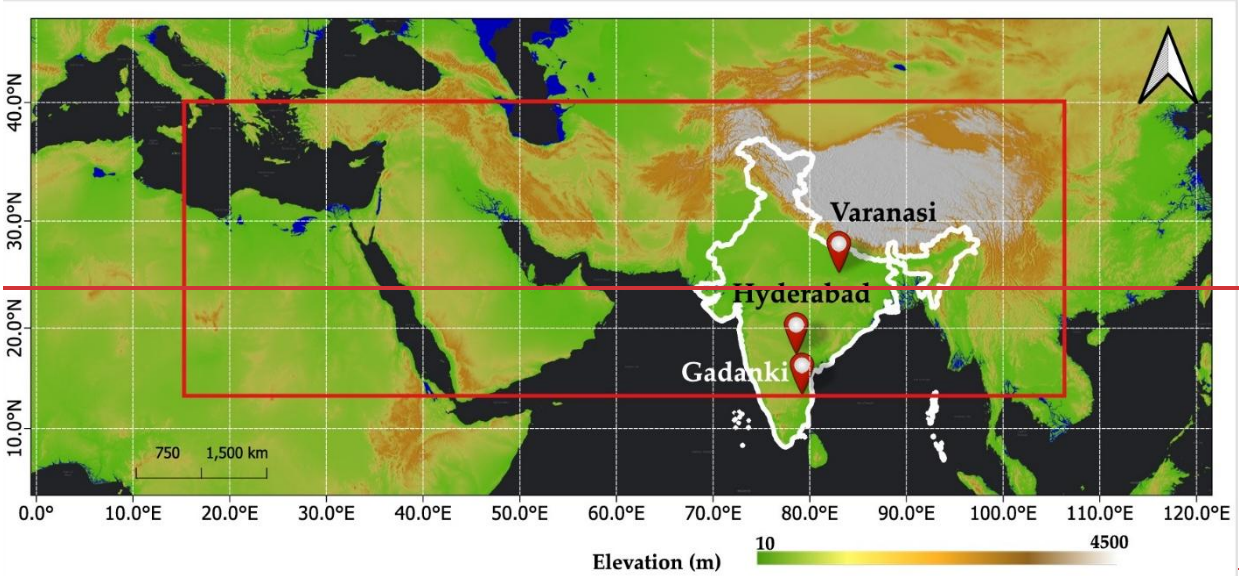

~~**Figure 1:** The balloon-launching locations during the 2014-2018 BATAL campaigns. The region~~

~~enclosed in the red color box is the typical geographic extent of the ATAL region (15°E to 105°E; 15° N to 40° N)~~

Table ~~1: The details~~**1:** Summary of balloon launches ~~and the payloads used~~during the BATAL campaigns, highlighting the availability of Compact Optical Backscatter Aerosol Detector (COBALD~~, Ozonesonde, and Radiosonde) in this study have~~), radiosonde, and ozonesonde measurements. All measurements cover a minimum ~~of 20 km~~ altitude ~~coverage~~of 20 km, with maximum altitudes ranging from ~~the surface. The letter~~25 to 35 km. The average maximum altitude is 29 km at Gadanki, 27 km at Hyderabad, and 30 km at Varanasi. 'Y' ~~denotes if the~~indicates data ~~from~~availability for a ~~particular~~specific payload~~ is available. Meanwhile, the letter~~, while 'N' denotes non-availability. All launches ~~are~~were conducted ~~in the~~during local ~~night-time~~nighttime (UTC +~~-~~05:30~~)~~).

~~Location~~	**~~Date (DD-MM-YYYY) and Time (UTC) of launch~~**	**~~COBALD~~**	**~~OZONE SONDE~~**	**~~RADIO SONDE~~**
Location	**Date and Time (UTC) of launch**	**COBALD**	**Ozonesonde**	**Radiosonde**
Gadanki **(13.48°N, 79.18°E)**	18-08-2014, 15:00	Y	N	Y
	19-08-2014, 15:30	Y	Y	Y
	07-09-2016, 19:50	Y	Y	Y
	09-09-2016, 15:00	Y	Y	Y
	31-07-2017, 18:00	Y	Y	Y
	01-08-2017, 18:00	Y	Y	Y
Hyderabad (17.47°N, 78.58°E)	01-08-2015, 17:00	Y	N	Y
	05-08-2015, 22:00	Y	Y	Y
	06-08-2015, 22:00	Y	Y	Y
	08-08-2015, 18:00	Y	N	Y
	09-08-2015, 22:00	Y	N	Y
	13-08-2015, 18:00	Y	Y	Y
	08-08-2018, 21:00	Y	Y	Y
	17-08-2018, 20:00	Y	Y	Y
	26-08-2018, 20:00	Y	Y	Y

	28-08-2018, 20:20	Y	Y	Y
Varanasi **(25.27°N, 82.99°E)**	22-08-2015, 18:00	Y	N	Y
	22-08-2015, 22:00	Y	N	Y
	04-08-2016, 23:00	Y	N	Y
	06-08-2016, 21:00	Y	Y	Y
	08-08-2016, 21:30	Y	Y	Y

~~***3.1. Radiosonde and Ozonesonde***~~

~~We utilized pressure, temperature, and relative humidity (RH) data from radiosondes and ozone volume mixing ratios from ozonesondes. The Meisei (RS-11 G) and iMet radiosondes were used to measure temperature and pressure at different altitudes. The iMet radiosondes used piezo-resistors for atmospheric pressure measurements with an accuracy of 1-2 hPa. The Meisei radiosonde, which lacks a pressure sensor, calculated pressure using temperature and GPS altitude data. The ozone profile was obtained using EN-SCI Electrochemical Concentration Cell (ECC) ozonesondes, following the method by Komhyr et al. (1995). More details on these methodologies are available in Ratnam et al. (2014) and Akhil Raj et al. (2015).~~

~~Relative humidity and ozone mixing ratios were converted to absolute densities using equations described by Santhosh et al. (2024a). **Fig. 2** shows the extracted mean profiles of pressure, temperature, water vapor density, and ozone density over the entire study period across the locations. We found that the temperature, water vapour density, and ozone density measurements vary across the locations, while the differences in the pressure measurements are negligible. We have seen the range of water vapour measurements over Varanasi at below boundary layer (altitude < 2 km), free troposphere (2 to 12 km) and UTLS (12 to 20 km) altitudes are higher (13 to 21 g m^{-3}, 60 mg m^{-3} to 13 g m^{-3}, and 0.4 to 60 mg m^{-3}, respectively) in comparison~~

~~with Gadanki (12 to 19 g m^{-3}, 30 mg m^{-3} to 11.7 g m^{-3}, and 0.9 to 30 mg m^{-3}, respectively) and Hyderabad (11.3 to 17 g m^{-3}, 44 mg m^{-3} to 10.75 g m^{-3}, and 0.4 to 40 mg m^{-3}, respectively). Similar way, the ozone measurements within the boundary layer, free troposphere, and UTLS were also higher over Varanasi (0 to 61 µg m^{-3}, 34 µg m^{-3} to 61 µg m^{-3}, and 34 to 215 µg m^{-3}, respectively) in comparison with Gadanki (0 to 50 µg m^{-3}, 30 µg m^{-3} to 50 µg m^{-3}, and 30 to 160 µg m^{-3}, respectively) and Hyderabad (5.3 to 39 µg m^{-3}, 28.2 µg m^{-3} to 39.1 µg m^{-3}, and 29 to 176 µg m^{-3}, respectively). Regarding temperature, Varanasi profiles were warmer than the other locations, especially in the UTLS region (208.9 to 230 K) compared to Hyderabad (207.12 to 227.3 K) and Gadanki (205.3 to 226 K).~~

3.3.~~We also assessed the biases in these measurements by comparing them with data from the Microwave Limb Sounder (MLS), Atmospheric Infra-Red Sounder (AIRS), and Modern-Era Retrospective analysis for Research and Applications, Version 2 (MERRA-2). The biases ranged from -5 to 5 hPa (-1.5 to 1.5 %) for pressure, -5 to 5 K (-3 to 3%) for temperature, -2 to 2 gm^{-3} (-150 to 150%) for water vapor density, and -50 to 40 (-100 to 40%) µg m^{-3} for ozone density. It must be noted that the satellite and reanalysis measurements show higher biases at higher altitudes, and this is discussed in detail by Santhosh et al. (2024a), which makes the~~

Ancillary Datasets

-In addition to in-situ measurements~~ more reliable at these altitudes~~

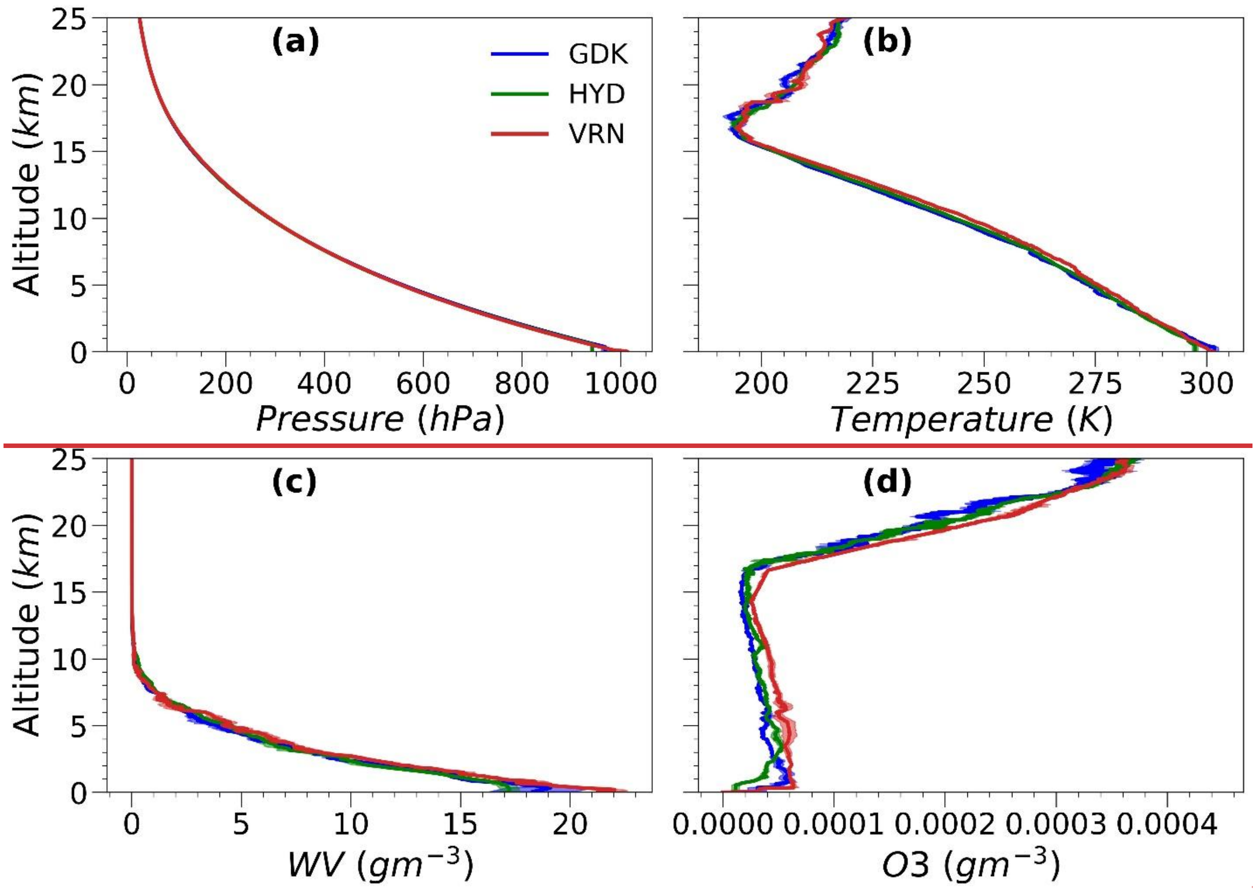

~~**Figure 2:** The mean profiles of (a) pressure, (b) temperature, (c) water vapor density (WV), and (d) ozone density (O3) with ±1σ standard errors across~~, we utilized the ~~study locations.~~following ancillary datasets:

~~***3.2. Compact Optical Backscatter AerosoL Detector (COBALD)***~~

~~COBALD is a lightweight balloon-borne sonde developed by ETH Zurich that measures backscattered light from aerosols, molecules, and clouds. This sonde was designed for nighttime operation only and uses two LED light sources emitting at 455 nm and 940 nm wavelengths. It detects backscattered light from particles up to 10 meters away, with a precision better than 1% in~~

~~the UTLS region (Ravi Kiran et al., 2022; Vernier et al., 2015; 2018). Data are transmitted in real-time along with pressure and temperature readings at a frequency of 1 Hz.~~

~~1.1. 3.3. Other Ancillary Datasets~~

~~3.3.1.~~ MERRA-2 Reanalysis ~~Data~~

(i) : We used the Modern-Era Retrospective analysis for Research and Applications, Version 2 (MERRA-2), Hourly, Time-averaged, Single-Level, Assimilation, Aerosol Diagnostics dataset (M2T1NXAER; 0.~~625° X~~625° × 0.~~5°~~5° resolution, V5.12.4 ~~(M2T1NXAER) product~~) developed by NASA’s Global Modelling and Assimilation Office (GMAO) ~~for retrieving the~~to retrieve AOD values for the campaign period. ~~This dataset was chosen as there~~These AOD values were ~~no~~used to normalize aerosol extinction profiles, ensuring consistency between columnar aerosol loading and derived extinction profiles (for example, Santhosh et al., 2024b). Since collocated nighttime AOD retrievals ~~of AOD~~ from in-situ measurements~~. Further,~~ were unavailable, MERRA-2 served as a reliable alternative. Che et al. (2019) reported ~~the~~improved MERRA-2 AOD performance ~~of the MERRA-2 AOD measurements is better~~ in the South Asian region ~~(correlation coefficient, r = 0.84; root-mean-square error, RMSE = 0.18; mean absolute error, MAE = 0.11 and mean fractional error, MFE = 34.54%)~~ based on ~~the comparison~~comparisons with AERONET observations ~~on a global scale making it a suitable alternative when the ground-based retrievals are unavailable. It~~. The dataset provides total ~~aerosol optical depth (AOD)~~AOD at 550 nm and the Angstrom exponent (AE) ~~in~~for the 470-870 nm ~~region~~range. The AODs at 455 and 940 nm wavelengths were derived using the Angstrom power law (Angstrom, 1964~~) given by~~):

$$AOD_{\lambda_0} = \cancel{AOD_{550}\left(\frac{\lambda_0}{550}\right)^{-AE}} AOD_{550} \times \left(\frac{\lambda_0}{550}\right)^{-AE} \tag{1}$$

where λ0 represents the ~~required~~target wavelength. ~~As~~Given that our required wavelengths ~~are just~~(455 nm and 940 nm) fall slightly outside the ~~wavelength~~470-870 nm range~~ of the Angstrom exponent (-25 nm in the blue region and +70 nm in the red region), calculations beyond this range assume that the same ~~, we assumed the power-law relationship ~~holds.~~remains valid. Across ~~the ~~study locations, Varanasi had the highest mean nighttime AOD at 550 nm (0.37 ± 0.13~~),~~) from 19:30 to 05:30 local time, followed by Hyderabad (0.28 ± 0.05) and Gadanki (0.26 ± 0.07). ~~The Angstrom exponent (AE) was highest in Varanasi, indicating a greater fine mode aerosol contribution, while Hyderabad had the lowest AE, suggesting coarse-mode dominance. The AE over Gadanki indicated a more complex aerosol mix. We have identified the most likely aerosol types in the boundary layer and free troposphere over all three locations using the cluster analysis of the seven days of air mass back trajectories at 500 m and 4000 m a.m.s.l with HYbrid Single Particle Lagrangian Integrated Trajectory (HYSPLIT) model (Draxler & Hess, 1998).~~

~~*3.3.2.*~~ **Moderate Resolution Imaging Spectroradiometer (MODIS~~)~~**

(ii)): Surface reflectance is a critical parameter in ~~estimating the ~~aerosol radiative forcing~~.~~ calculations. We used the MCD43A4 Nadir Bidirectional Reflectance Distribution Function (BRDF)-Adjusted Reflectance (NBAR) product. This ~~product~~dataset (MODIS/Terra Nadir BRDF-Adjusted Reflectance Daily L3 Global 500m SIN Grid) provides spectral reflectance ~~for each~~values at MODIS spectral band (centered at 0.469, 0.555, 0.645, 0.859, 1.24, 1.64, and 2.13 µm) at local solar noon (~~https://lpdaac.usgs.gov/product/mcd43a4v061~~https://lpdaac.usgs.gov/product/mcd43a4v

061). ~~We found similar surface~~Surface reflectance values were found to be similar across ~~the~~study locations in the visible spectrum, with ~~some~~ deviations in the infrared ~~region, where~~range. Among the sites, Hyderabad ~~had~~exhibited the highest reflectance~~ and~~, while Varanasi had the lowest (**Fig.** ~~S1~~S2).

~~4. Methodology~~

4. ~~A schematic of the~~ Methods

The methodology ~~used~~followed in this study ~~is shown in~~ (**Fig.** ~~3, and the steps involved are~~ 2) is discussed in the following subsections.

4.1.~~*4.1. In situ aerosol extinction from*~~ Cloud Screening of the COBALD ~~*measurements*~~Profiles

~~As~~ COBALD measurements capture ~~the~~ total backscattered light from a ~~mix~~mixture of aerosols, clouds, and molecules~~, isolating~~. Isolating aerosol ~~contribution~~contributions from the total backscatter ~~will be difficult when~~ becomes challenging in the presence of clouds~~ are present~~, necessitating the identification and exclusion of these cloud-contaminated in-situ measurements. The total backscatter signal is typically expressed ~~in terms of~~as the backscatter ratio (BSR~~) given by the following equation~~), defined as:

$$BSR = \frac{\beta_{Total}}{\beta_{mol}} \qquad (2)$$

where β_{mol} represents the molecular backscatter coefficient, ~~whereas the~~while β_{Total} includes both particle and molecular ~~contribution (in the absence of clouds). The contribution from molecular Rayleigh scattering~~contributions. In cloud-free conditions, $\beta_{Total} = \beta_{mol} + \beta_{aer}$, where β_{aer} is ~~determined using the radiosonde's simultaneous temperature and pressure recordings. The color index (CI) is defined as the 940-to-455nm ratio of~~ the aerosol ~~component of the BSR given by~~backscatter coefficient.

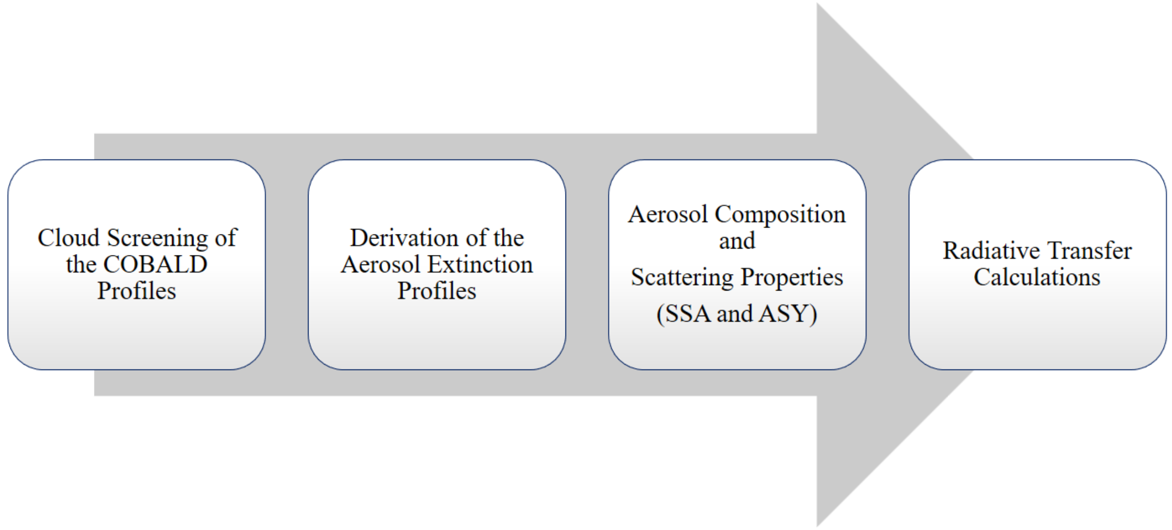

Figure 2: Schematic representation of the methodology used in this study. SSA and ASY refer to single scattering albedo and asymmetry parameter, respectively.

The color index (CI) is defined as the 940-to-455nm ratio of the aerosol component of BSR:

$$CI = \frac{BSR_{940}-1}{BSR_{455}-1} \qquad (3)$$

CI~~, being~~ is independent of particle number concentration~~, is~~ and serves as a useful metric for interpreting ~~the~~ particle size. Both BSR and CI ~~serve as~~are indicators of ~~the~~aerosol presence ~~of aerosols. For example, cirrus~~. Cirrus clouds can be ~~detected either~~identified separately ~~from blue and red channel~~ using BSR ~~measurements~~at 455 nm and 940 nm or ~~by taking advantage of the~~through CI, ~~enabling distinct~~which enables discrimination between ice particles (CI < 7) and aerosol (CI > 7~~), as highlighted in~~) (Hanumanthu et al., ~~(~~2020). ~~Considering these aspects~~Based on previous studies, we ~~used~~ set the following cloud screening criteria (above 10 km):

- BSR$_{455}$ < 1.12 for the blue channel measurements, similar to Akhil Raj et al. (2022~~) and set~~).
- BSR940 < 2.5 and CI > 7 for the red channel following Vernier et al. ~~(2015) for~~

~~screening the aerosols in the UTLS (above 10 km).~~ (2015).

Since ~~the above~~these cloud screening criteria ~~are~~have not ~~yet~~been validated ~~for screening aerosols~~ in the ~~troposphere~~lower atmosphere, we ~~used~~employed an alternative approach ~~combining both the~~that combines vertical gradients of air temperature and relative humidity (RH) ~~and the~~with altitude-dependent RH thresholds ~~of RH to determine the clouds in the lower and free troposphere~~, as described in Xu et al. ~~(2023). Note that we restricted~~(2023), in the lower atmosphere (below 10 km). While radiosonde data provide measurements in the UTLS and beyond, this ~~cloud screening~~ method ~~below 10 km owing to the high~~may introduce uncertainties at higher altitudes due to radiosonde limitations associated with ~~radiosonde~~ the accuracy of RH measurements ~~in probing RH beyond this altitude.~~(Miloshevich et al., 2006). A ~~brief~~detailed description of this method is provided in the ~~supplement~~Supplement (**Section S1**), along with relevant relative humidity (RH) thresholds (**Table S1**) and an example (**Fig. ~~S2~~S3**).

Based on the above methodology, a backscatter ratio profile influenced by molecules and aerosols is derived from the surface to the maximum altitude of a given COBALD measurement.

4.2. Derivation of the Aerosol Extinction Profiles

Under cloud-free conditions, the aerosol backscatter coefficient β_{aer} (expressed in m^{-1} sr^{-1}) at a given wavelength λ and altitude z is obtained from **Eq. (2)**:

$$\beta_{aer,\lambda}(z) = \beta_{mol,\lambda}(z) \times (BSR(z) - 1) \qquad (4)$$

The molecular backscatter coefficients ~~were~~ β_{mol} (expressed in m^{-1} sr^{-1}) are determined using the in-situ temperature and pressure profiles ~~obtained~~ from ~~the~~ radiosonde measurements (Collis and ~~Russel, 1976)~~Russell, 2005) using the following equation:

$$\beta_{mol,\lambda}(z) = \frac{P(z)}{R_d T(z) M}\left(\frac{\lambda}{550}\right)^{-4.09} \times 10^{-32} \cancel{m^{-1} sr^{-1}} \quad \cancel{(7),} \qquad (5)$$

where ~~λ is the given wavelength,~~ R$_d$ = 287 J K^{-}~~^{1}kg~~^{1} kg^{-1} is the gas constant for ~~the~~ dry air, and M = 4.81 ~~X 10^{-32}~~× 10^{32} kg is the molecular weight of dry air ~~expressed in kilograms. Using this, the aerosol backscatter coefficients are obtained below:~~

. ~~$\beta_{aer,\lambda}(z) = \beta_{mol,\lambda}(z)(BSR(z) - 1)$ (8)~~

The aerosol backscatter coefficients were ~~then~~ multiplied ~~with~~by a lidar ratio of 40 sr to ~~get the~~derive extinction coefficient profiles~~. This particular ratio was used by several~~, consistent with previous studies over the Indian region ~~for deriving the vertical extinction profiles from the backscatter profiles~~ (e.g.~~.~~., Gupta et al~~.~~., 2021). ~~Further, to overcome the limitation due to~~

To reduce uncertainties in lidar ratios, the aerosol extinction coefficient profiles ~~(~~β$_{ext}$ ~~(z~~))~~)~~) at ~~a given~~ wavelength ~~'λ' have been~~λ were normalized using ~~the~~ MERRA-2 AOD ~~(at 'λ') as~~:

$$\beta_{ext,scaled}(\lambda, z) = \beta_{ext}(\lambda, z) \times \frac{AOD_{MERRA-2}(\lambda)}{AOD_{COBALD}(\lambda)}$$

(~~9~~6)

where AOD$_{COBALD}$(λ) represents the AOD obtained by integrating the derived aerosol extinction ~~profiles at the given wavelength. This scaling also~~profile (with a lidar ratio of 40 sr). This normalization ensures consistency between the columnar loading and ~~the~~ extinction profiles ~~obtained which eventually helps to reduce the~~, reducing biases in the ~~ARF and HR~~ estimates of aerosol direct radiative effects (Santhosh et al., 2024b).

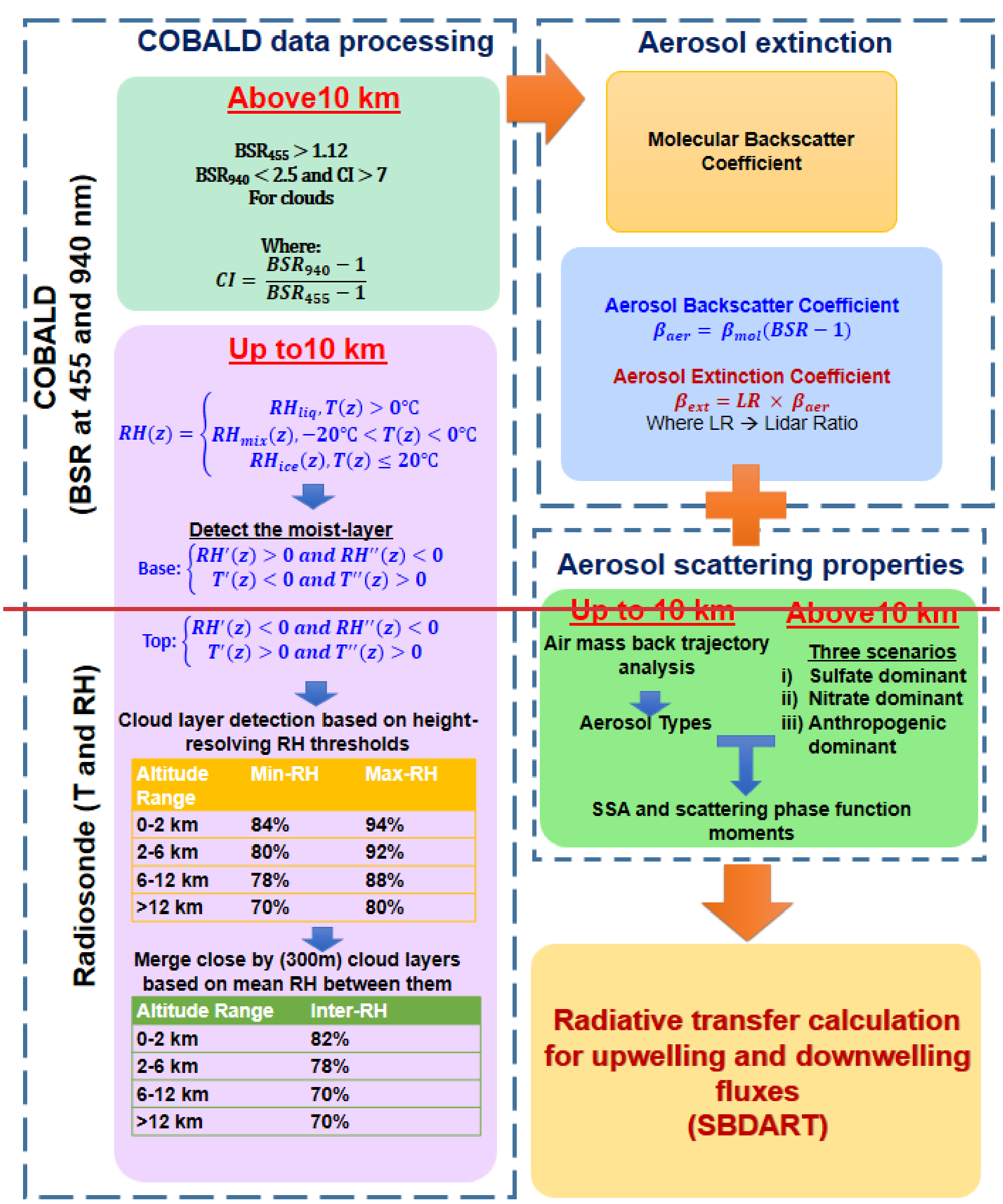

Altitude Range	Min-RH	Max-RH
0-2 km	84%	94%
2-6 km	80%	92%
6-12 km	78%	88%
>12 km	70%	80%

Altitude Range	Inter-RH
0-2 km	82%
2-6 km	78%
6-12 km	70%
>12 km	70%

~~**Figure 3:** The layout of the methodology used in this study~~

~~*4.2. Inferring aerosol types for scattering properties*~~

~~The balloon-borne measurements of Single Scattering Albedo (SSA) and Asymmetry parameter (ASY) are not possible. So, we adopted the following strategies for the possible aerosol types in the UTLS and below (within the boundary layer and free troposphere).~~

4.3.~~The aerosol composition of ATAL in the UTLS region remains uncertain and inconsistent. Earlier studies reported the presence of sulfates (Fadnavis et al., 2013; Li et al., 2005; Ma et al., 2019; Hopfner et al., 2019;~~ Aerosol Composition and Scattering Properties

The composition of aerosols in the UTLS region during ATAL periods remains highly variable across different measurement techniques and time periods, posing a significant challenge for accurate characterization (**Table 2**). Despite differences, multiple studies consistently report the presence of sulfates, nitrates, organic carbon, and ammonium aerosols in varying proportions.

Table 2: Summary of studies on ATAL aerosol composition using different models and measurement techniques.

~~Bossolasco et al. 2021), nitrates (Vernier et al. 2018; Hopfner et al. 2019; Ma et al. 2019; Fairlie et al. 2020; Vernier et al. 2022; Yu et al., 2022), and absorbing aerosols of anthropogenic origin transported from the lower troposphere (Li et al. 2005; Fadnavis et al. 2013; Lau et al. 2018; Bossolasco et al. 2021). Offline chemical analysis from BATAL revealed a dominant nitrate contribution (Vernier et al. 2018). Appel et al. (2022) argued that ATAL consisted solely of secondary substances, namely an internal mixture of nitrate, ammonium, sulfate, and organic matter. Considering all together, we assumed three different scenarios of aerosols, say, sulfates, nitrates, and minimum to non-absorbing mixed-type, are dominant in the UTLS region.~~

~~(a) A Sulfate aerosol model consisting of 75% H_2SO_4 serves as a typical background aerosol (Hess et al., 1998).~~

~~(b) Nitrate aerosol model (Zhang et al., 2012) with dominant accumulation mode following a log-normal size distribution (mode radius:0.15 µm, standard deviation: 1.9). This assumption is consistent with the inferences from the StratoClim field campaigns (Mahnke et al., 2021), where they noticed the main mode of the aerosol size distribution~~

~~shifts towards the accumulation mode with increase in the altitude from beneath the lower edge of ATAL. Further, they detected the vertical particle mixing ratio within the ATAL ~700 mg^{-1} for the particles in the size range 65 nm to 1μm and a higher mixing ratio (>2500 mg^{-1}) for the particles whose diameters are larger than 10 nm. They also noticed that the particles below the ATAL are influenced by the nucleation of aerosol particles (diameter < 65 nm).~~

~~(c) The minimum absorbing mixed-type aerosol model includes the anthropogenic contribution and is represented by the continental clean type of aerosols (Hess et al., 1998). This aerosol type encompasses continental regions with minimal to no anthropogenic influence, typically containing less than 0.1 μg m^{-3} of soot. Its composition consists of slightly dominant water-soluble aerosols (59%) and insoluble aerosols (41%). The water-soluble part of aerosol particles originates from gas-to-particle conversion and consists of sulfates, nitrates, organic, and other water-soluble substances. Thus, it can be used to describe anthropogenic aerosol, which is just beyond the sulfates. The water-insoluble part of aerosol particles, on the other hand, consists of a certain amount of organic material together with soil particles. Thus, despite two of our study locations (Hyderabad and Varanasi) being heavily urbanized with a high likelihood of anthropogenic emissions lifting towards the UTLS, the assumption of a continental clean aerosol model sets a baseline for anthropogenic aerosols with minimal absorption in the solar spectral range. Hereafter, we denote the continental clean as 'ANTH' as it's a baseline for the anthropogenic/absorbing type of aerosols. Earlier, Gadhavi and Jayaraman (2006) also used this aerosol model together with sulfate~~

~~aerosol models in the stratosphere to estimate the aerosol radiative forcing over Hyderabad.~~

~~The RH-specific SSA and ASY values of Sulfate (SUL), Nitrate (NIT), and Anthropogenic (ANTH) aerosols at wavelengths of 455 nm and 940 nm (**Fig.4**) were assigned to corresponding altitude bins based on their respective RH levels to obtain the profiles of SSA and ASY in the UTLS.~~

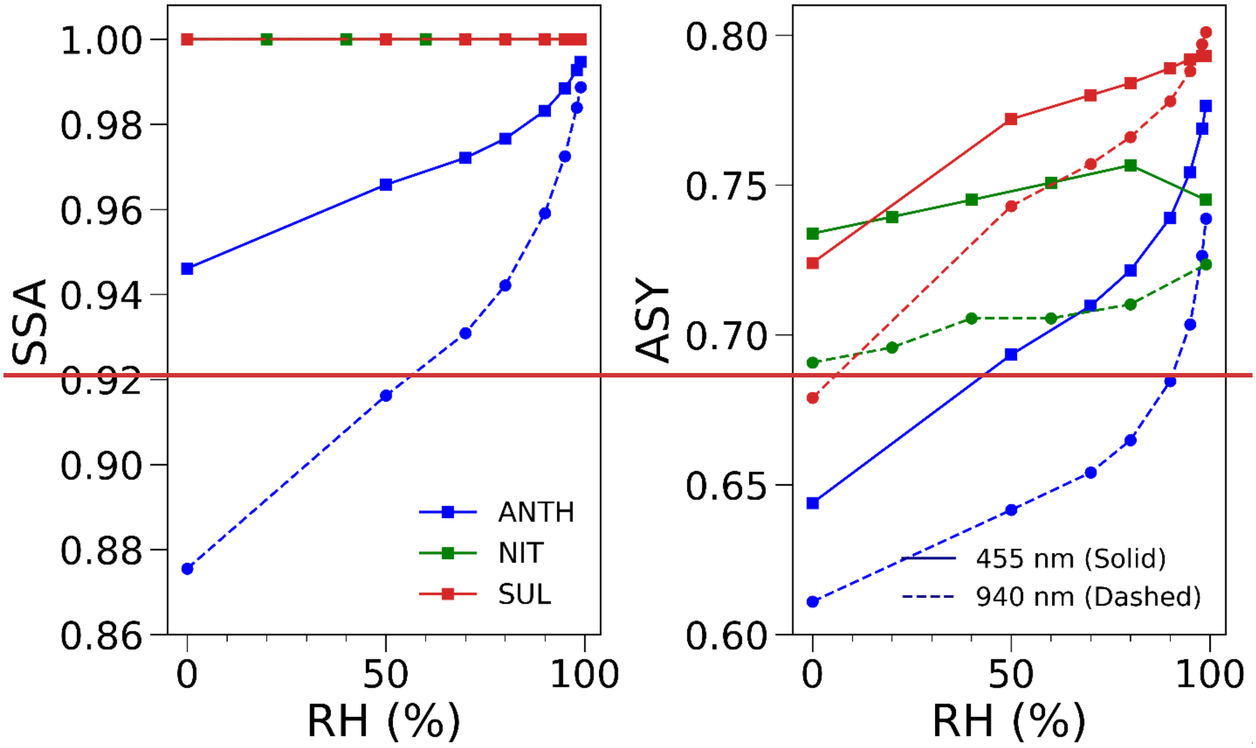

~~**Figure 4**: The variation of SSA and ASY for the three dominant categories of UTLS, namely anthropogenic (ANTH), nitrate (NIT), and sulfate (SUL) at different RH bins.~~

~~To determine the likely aerosol types within the boundary layer (WBL) and free troposphere (FT), we used the clustered mean seven-day air mass back trajectories at 500 m and 4000 m a.m.s.l to represent the region within the boundary layer and free troposphere, respectively, over the study locations using HYSPLIT (Stein et al., 2015) The clustering has been~~

~~done for every air mass for the campaign period at a given location. The aerosol type classification in this way mainly depends on the air mass origins, region of transport, the residence time of air masses in a particular area, the altitude of the air mass above the ground level, and the location of the experiment together with the altitude at which the air masses are terminated. We have classified the major air mass origins over the study locations as below:~~

~~(a) A northwest/west (NW/W) sector that includes the North African countries, Arabian Peninsula, northwestern India (Thar desert), and other Asian countries (such as Pakistan and Afghanistan) that expect to contribute dust aerosols.~~

~~(b) A northern sector (N), mostly the IGP, with air masses containing highly polluted aerosols~~

~~(c) Eastern (E) sector with the air masses mostly from the Bay of Bengal of oceanic origin~~

~~(d) Southern (S) sector with the air masses are mostly of oceanic origin;~~

~~(e) Central and Peninsular India (C), where the aerosols are moderately polluted in comparison with the northern sector~~

~~(f) Local (L) sector in and around the study location where the types of emissions are heavily dependent on the degree of urbanization.~~

~~A similar approach in this way has been made previously by Pawar et al., (2015) over Pune to obtain the aerosol types from back trajectory analysis. The aerosol types are defined based on Hess et al. (1998) and brief descriptions of these types are provided in the supplement (**Section S2 and Fig. S3**). The obtained back trajectory clusters and the assigned aerosol types for three locations are given respectively in **Fig. 5** and **Table 2**. It is also important to note that the scale height of marine aerosols is typically small (less than 2 km); therefore, we only considered this type within~~

~~the boundary layer. Additionally, air masses of oceanic origin that remain on land for more than 24 hours before reaching their destinations are classified as aerosols of continental or local origin.~~

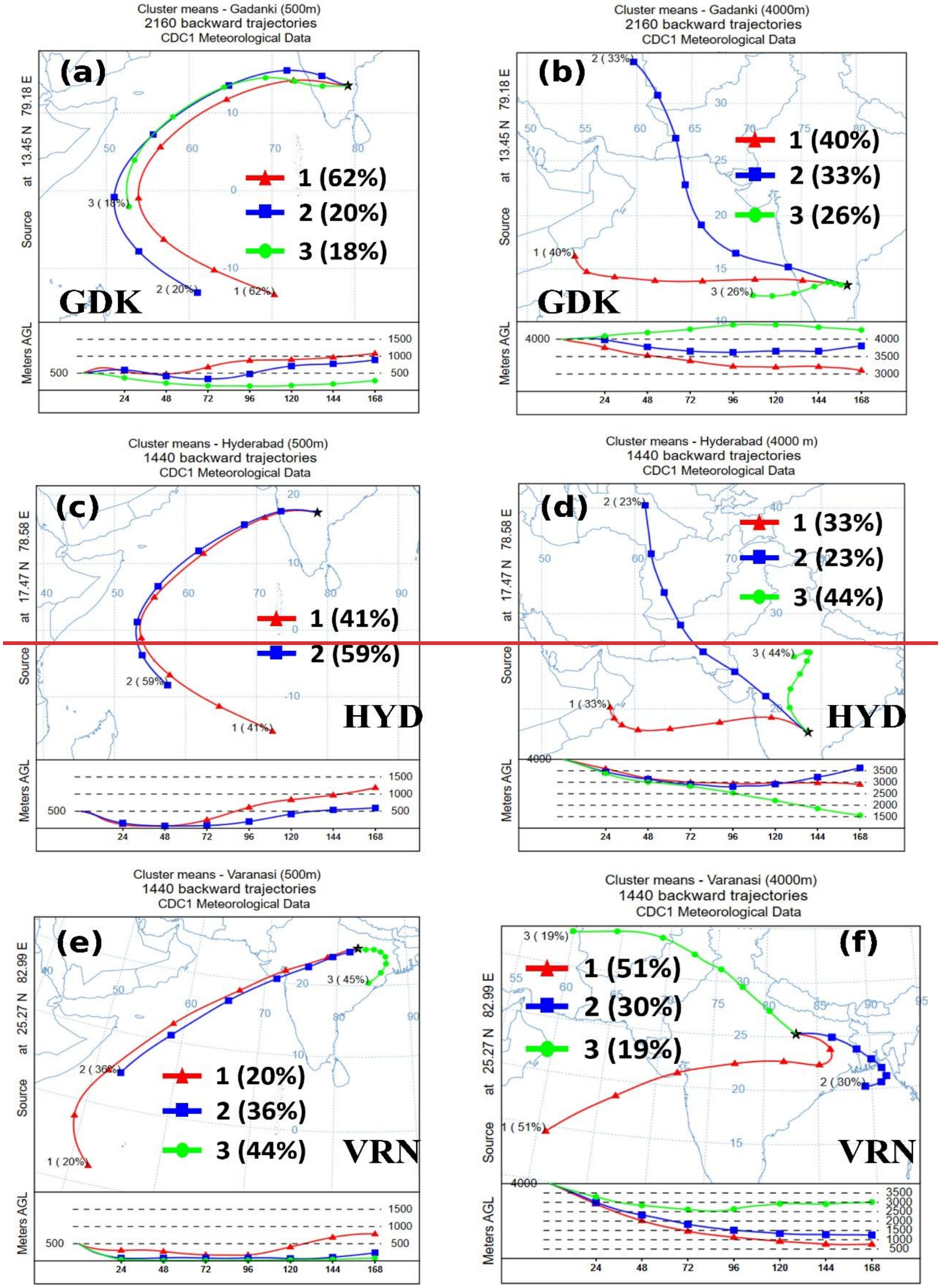

~~**Figure 5:** The seven-day air mass back trajectory clusters were analyzed at 500 m and 4000 m above ground level at Gadanki (GDK) (a, b), Hyderabad (HYD) (c, d), and Varanasi (VRN) (e, f).~~

~~**Table 2:** Identified aerosol types based on the cluster analysis of air mass back trajectories at the three locations.~~

~~Location~~Study Method and Period	**~~Within Boundary Layer (500m)~~Aerosol Composition at the UTLS**	**~~Free Troposphere (4 km)~~Reference**
~~Gadanki~~Coupled Aerosol – Radiation – Earth System Model (2015, 2017, 2021)	~~Maritime Tropical (62%)~~ ~~Continental Average (38%)~~Nitrate, Organics, Sulfate, Ammonium aerosols between 15°N–45°N and 0°E–160°E	~~Desert (72%)~~ ~~Continental Average (27%)~~Zhu et al. (2024)
~~Hyderabad~~Aircraft measurements (2017)	~~Urban (59%)~~ ~~Maritime Polluted (41%)~~Nitrate, Ammonium, Sulfate, and Organic Carbon	~~Polluted Continental (44%)~~ ~~Desert (56%)~~Appel et al. (2022)
Offline ion chromatography (2017)	Nitrate and Nitrite aerosols	Vernier et al. (2022)
~~Varanasi~~Earth System Model (2017 – 2021)	~~Urban (60%)~~ ~~Continental Average (20%)~~ -Nitrate (~30 – 40 %), Nitric Acid	~~Desert (19%)~~ ~~Continental Average (51%)~~ ~~Continental Polluted (30%)~~Yu et al. (2022)
Earth System Model (2000 – 2015)	Sulfate (40%), secondary + primary organics (45%), Ammonium (14%), Trace (less than 3%) amount of BC	Bossolasco et al. (2021)
Chemical Transport Model (2013)	Organic Carbon, Nitrate, Sulfate, Ammonium	Fairlie et al. (2020)
Atmospheric Chemistry and General Circulation Model	Mineral Dust, Water Soluble (Sulfate and Nitrate) aerosols	Ma et al. (2019)
Satellite + Aircraft + Trajectory simulations + Cloud Chamber experiments (1997, 2002 – 2012, 2017)	Ammonium Nitrate	Hopfner et al. (2019)

~~After obtaining the percentage contribution of each aerosol type in the boundary layer and free troposphere, we computed the SSA and ASY based on the RH at a given altitude. Suppose N_i is the fraction of a given aerosol type. In that case, N_f is the total number of aerosol types, and N is the sum of the fractions of all aerosol types at a given altitude bin (z). SSA and ASY for each wavelength are obtained according to RH at that particular altitude bin as follows:~~

~~$SSA(z) = \sum_{i=1}^{Nf} \frac{N_i * SSA_i}{N}$ (10)~~

~~$ASY(z) = \sum_{i=1}^{Nf} \frac{N_i * SSA_i * ASY_i}{N_i * SSA_i}$ (11)~~

~~***4.3.***~~To account for this variability, we considered seven UTLS aerosol scenarios with different fractions of sulfate (SUL), nitrate (NIT), organic carbon (OC), and ammonium (AM), assuming external mixing (**Table 3**). Among these scenarios, the OC-dominant combination (with 50% OC, denoted as C1) and the combination with 40% OC and 30% AM (denoted as C2) are adapted, respectively, from Bossolasco et al. (2021) and Appel et al. (2022). Two ideal scenarios are also assumed where the sulfate and nitrate aerosols contribute 100% of the UTLS aerosols (SUL and NIT, respectively). The SUL scenario serves as a reference, representing UTLS aerosols with background sulfate levels similar to those in the stratosphere (Junge and Manson, 1961). The NIT scenario defines an upper baseline, while the remaining cases (denoted as C1 to C5) explore varying nitrate compositions from 0 to 0.4.

Table 3: Aerosol mixing scenarios considered for UTLS aerosols, with fractional compositions (f_i) of sulfates (SUL), nitrates (NIT), organic carbon (OC), and ammonium sulfate (AM).

Combination	**Fractional composition (f_i)**			
	SUL	**NIT**	**OC**	**AM**
SUL	1	0	0	0
NIT	0	1	0	0

C1[*]	0.4	0	0.5	0.1
C2[**]	0.1	0.2	0.4	0.3
C3	0.2	0.3	0.3	0.2
C4	0.1	0.4	0.2	0.3
C5	0.2	0.3	0.1	0.4

** This combination is adapted from Bossolasco et al. (2021)*

***This combination is adapted from Appel et al. (2022)*

The SSA and ASY of each aerosol species were derived from their size distribution parameters and complex refractive indices under dry conditions (**Table S2**) using the Mie scattering theory, assuming that all the aerosol species follow the log-normal size distribution. If f_i is the fraction of an individual aerosol species in a given combination, then SSA and ASY of the combination are obtained using the following equations:

$$SSA(\lambda) = \frac{\sum_i f_i SSA_i(\lambda)}{\sum_i f_i} \qquad (7)$$

$$ASY(\lambda) = \frac{\sum_i f_i ASY_i(\lambda)}{\sum_i f_i} \qquad (8)$$

where SSAi and ASYi denote the single scattering albedo and asymmetry parameter of respective aerosol species at a given wavelength λ. These derived SSA and ASY for each aerosol combination at 455 and 940 nm are illustrated in **Figure 3**.

Among the compositions, the OC-dominant scenario (C1) exhibits the lowest SSA, indicating higher absorption, while SSA increases with decreasing OC fractions and increasing fractions of nitrates and ammonium (C2- C5). Sulfates and nitrates have SSA=1 at both wavelengths (445 nm and 940 nm), with slight ASY differences (e.g., ASY_{SUL} = 0.724, ASY_{NIT} = 0.718 at 445 nm and ASY_{SUL} = 0.679, ASY_{NIT} = 0.549 at 940 nm). These SSA and ASY values were applied to altitude bins in the 10- to 20-km range.

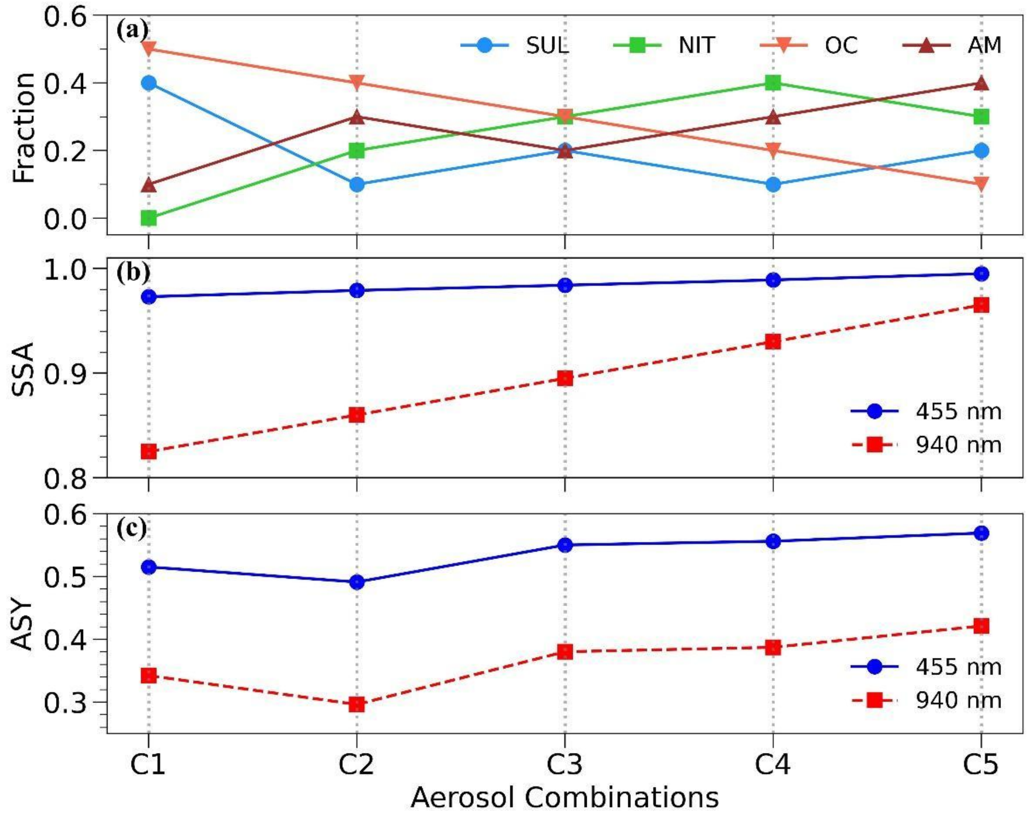

Figure 3: (a) Fractional contribution of aerosol species—sulfate (SUL), nitrate (NIT), organic carbon (OC), and ammonium (AM)—in the aerosol mixing combinations (C1 to C5) considered in this study. (b) Single Scattering Albedo (SSA) and (c) Asymmetry Parameter (ASY) corresponding to each combination under dry conditions.

In the lower atmosphere (below 10 km), aerosol composition/typing was characterized using seven-day air mass back trajectories at 500 m (boundary layer) and 4000 m (free troposphere) above mean sea level, generated using the HYbrid Single Particle Lagrangian Integrated Trajectory (HYSPLIT) model (Stein et al., 2015). Trajectories were clustered based on spatial similarity using hierarchical clustering and the Total Spatial Variance (TSV) method, optimizing the number of clusters where further TSV reduction provides minimal improvement. This approach identifies distinct transport pathways shaped by synoptic-scale meteorology, allowing the classification of aerosol types based on air mass origin, transport history, and residence time over source regions.

A similar approach was used by Pawar et al. (2015) in Pune to identify aerosol types through back trajectory analysis. After categorizing the air-mass clusters based on potential aerosol types from the Optical Properties of Aerosols and Clouds (OPAC) database (Hess et al., 1998; **Table S3**), the corresponding wavelength and RH-dependent aerosol scattering properties (SSA and ASY) were obtained. A detailed description of this method is provided in **Section S2** (Supplementary Information) along with the identified aerosol types through back trajectory clusters at the three locations for the two altitude levels (**Figure S4**). Since marine aerosols typically have a low scale height (< 2 km), their influence was considered only within the boundary layer. Additionally, air masses of oceanic origin that remained over land for more than 24 hours before arrival were reclassified as continental aerosols.

4.4. Radiative Transfer Calculations

The radiative forcing due to aerosols at a given level of the atmosphere is the difference between the radiative fluxes under aerosol-laden and no-aerosol (and without clouds) conditions. For a given layer in the atmospheric column with its vertical thickness Δz (in km), this radiative forcing (RF, in W m^{-2}) at its top and bottom levels is mathematically expressed as:

$$RF_{Top} = \left(F_{wa}^{\downarrow} - F_{wa}^{\uparrow}\right)_{Top} - \left(F_{na}^{\downarrow} - F_{na}^{\uparrow}\right)_{Top} \tag{9}$$

$$RF_{Bot} = \left(F_{wa}^{\downarrow} - F_{wa}^{\uparrow}\right)_{Bot} - \left(F_{na}^{\downarrow} - F_{na}^{\uparrow}\right)_{Bot} \tag{10}$$

Here, $F_{wa}^{\downarrow}$ and $F_{wa}^{\uparrow}$ represent the downward and upward radiative fluxes in aerosol-laden conditions, while $F_{na}^{\downarrow}$ and $F_{na}^{\uparrow}$ denote the corresponding fluxes under no-aerosol (and without clouds) conditions.

The Aerosol Radiative Forcing (ARF) of this atmospheric layer is the difference between the RF at its top and bottom levels, which quantifies the amount of energy trapped within the layer and represents the atmospheric absorption due to aerosols (Gadhavi and Jayaraman, 2006).

Mathematically,

$$ARF \equiv \Delta RF = RF_{Top} - RF_{Bot} \qquad (11)$$

The rate at which the atmosphere heats up due to aerosols (referred to as HR, in K day^{-1}) for a given layer can be determined using the following equation (Liou, 2002):

$$HR = \frac{\partial T}{\partial t} = \frac{g}{C_p}\left(\frac{\Delta RF}{\Delta P}\right) = \frac{-1}{\rho C_p}\left(\frac{\Delta RF}{\Delta z}\right) \qquad (12)$$

In this equation, g represents the acceleration due to gravity, and C_p denotes the isobaric specific heat capacity of dry air (~ 1006 J Kg^{-1} K^{-1}). ΔP signifies the pressure difference between the top and bottom boundaries of the atmospheric layer, ρ indicates the density of the air (in kg m^{-3}), and ΔRF/Δz represents the radiative power absorbed or emitted by the medium per unit volume of the atmosphere (in W m^{-3}). Since the atmosphere consists of several vertically heterogeneous layers, repeating the above calculation for each layer yields the profile of the heating rate.

For estimating the radiative forcing and heating rates associated with UTLS aerosols, ~~we have incorporated~~ the aerosol ~~data along with~~profiles (extinction coefficient, SSA, and ASY) and the atmospheric ~~parameters and other relevant information~~profiles (pressure, temperature, water vapor density, and ozone density) are provided as input into the Santa Barbara DISORT (discrete ordinate radiative transfer) Atmospheric Radiative Transfer (SBDART) model (Ricchiazzi et al. 1998). This computational tool calculates plane-parallel radiative transfer in various atmospheric and surface conditions, including clear and cloudy scenarios. The DISORT module, which employs a numerically stable algorithm, is used to solve the equations of plane-parallel radiative transfer in vertically inhomogeneous atmospheres (Stamnes et al~~.~~., 1988). The accuracy of the SBDART model is estimated to be within a few percent for clear-sky conditions~~ (with aerosols), approximately 10% for cloudy-sky predictions of surface irradiance in the visible spectrum, and possibly as low as 50% for cloudy-sky simulations in the near-infrared. We performed our~~

~~calculations in the SW region (0.25–4 μm) with a spectral resolution of 0.005 μm. The difference between the downward and upward radiative fluxes in aerosol-laden ($F_{wa}^{\downarrow}$ and $F_{wa}^{\uparrow}$ respectively) and no-aerosol (and without clouds) ($F_{na}^{\downarrow}$ and $F_{na}^{\uparrow}$, respectively) at the top of the atmosphere (TOA) and the surface of the atmospheric column (SUR) is referred to as radiative forcing due to aerosols (ARF) at those respective levels. This difference is mathematically expressed as: ~~.

~~$ARF_{TOA} = \left(F_{TOA,wa}^{\uparrow} - F_{TOA,wa}^{\downarrow}\right) - \left(F_{TOA,na}^{\uparrow} - F_{TOA,na}^{\downarrow}\right)$ (12)~~

~~$ARF_{SUR} = \left(F_{SUR,wa}^{\uparrow} - F_{SUR,wa}^{\downarrow}\right) - \left(F_{SUR,na}^{\uparrow} - F_{SUR,na}^{\downarrow}\right)$ (13)~~

The ~~atmospheric forcing due to aerosols can be then computed as:~~

~~$ARF_{ATM} = ARF_{TOA} - ARF_{SUR}$ (14)~~

~~Apart from this, we have also calculated the forcing within the boundary layer (from 0 to 2 km) by replacing the TOA to the top of the boundary layer (at 2 km) in equations (12) and (14); and at the free troposphere (from 2 to 12 km) by replacing TOA to top of the free troposphere (at 12 km) and SUR to bottom of the free troposphere (at 2 km) in (12), (13), and (14). Similarly, the UTLS forcing is also calculated within the layer from 12 to 20 km.~~

~~The ARF ~~calculations are performed ~~using~~in the shortwave (SW) region (0.25–4 μm) with a spectral resolution of 0.005 μm and 8 radiation streams at 1-h intervals for a range of solar zenith angles to obtain a 24-hour average. Shortwave ARF is computed for both the atmospheric column (extending from the surface at 0 km up to 30 km) and specifically for the UTLS region (12–20 km). Additionally, heating rate profiles are derived for the UTLS layer across all seven previously discussed aerosol scenarios.

~~The rate at which the atmosphere heats up due to aerosols (referred to as HR, in K day^{-1}) for each layer between the TOA can be determined using the following equation (Liou, 2002):~~

~~$HR = \frac{\partial T}{\partial t} = \frac{g}{C_p}\left(\frac{\Delta F_{ATM}}{\Delta P}\right) = \frac{-1}{\rho C_p}\left(\frac{\Delta F_{ATM}}{\Delta z}\right)$ (11)~~

~~In this equation, ‘g’ represents the acceleration due to gravity, and ‘C_p’ denotes the isobaric specific heat capacity of dry air (~ 1006 J Kg^{-1} K^{-1}). ‘ΔP’ signifies the pressure difference between the TOA and SUR boundaries of the atmospheric layer, ‘ρ’ indicates the density of the air (in kg m^{-3}), and ‘$\Delta F_{ATM}/\Delta z$’ represents the radiative power absorbed or emitted by the medium per unit volume of the atmosphere (in Wm^{-3}). Since the atmosphere consists of several vertically heterogeneous layers, repeating the above calculation for each layer yields the profile of the heating rate profile.~~

5. ~~5.~~ Results and Discussions

5.1.~~*5.1.*~~ Spatial ~~*variability*~~Variability of ATAL Aerosols in the UTLS Region

~~Fig. 6 shows~~**Figure 4** presents the mean cloud-screened ~~Backscatter Ratio~~backscatter ratio at 455 nm (BSR455) ~~profiles~~ for the UTLS region over ~~our~~the study locations.

~~To~~The approximate ~~the~~vertical extent of the ATAL region ~~in the UTLS, we utilized the methodology described by~~ is adapted from Akhil Raj et al. (2022~~). According to their approach, the ATAL region’s extent is determined from~~), where its boundaries are determined based on dynamic constraints. The lower boundary corresponds to the convective outflow level~~–~~, identified ~~by~~as the ~~minimum gradient of~~altitude where the potential temperature gradient reaches a minimum below the cold point tropopause (CPT) after ~~smoothing the~~applying a nine-point running mean~~-up to the layer~~. The upper boundary is defined by the altitude of maximum stability (L_{maxS}), derived from the ~~square of~~squared Brunt- Väisälä frequency (N^2). Their ~~findings indicate~~ analysis indicates that L_{maxS} is located 1–2.7 km above the ~~cold point tropopause~~CPT, corresponding to ~~the~~a potential temperature of approximately 442.11 ± 25.64 K (454.39 ± 13.89 K) over the Indian region, roughly

19 km above the Earth's surface. The convective outflow level, ~~however~~on the other hand, is ~~approximately~~observed at ~ 13 km across all ~~the~~ locations. ~~Therefore~~Based on these criteria, we ~~defined~~define the ATAL region's approximate vertical extent ~~of the ATAL region as ranging from~~between 13 km to 19 km~~ 13 km~~, corresponding to ~~19 km (350 K to 440 K~~a potential temperature~~).~~ range of 350 K to 440 K.

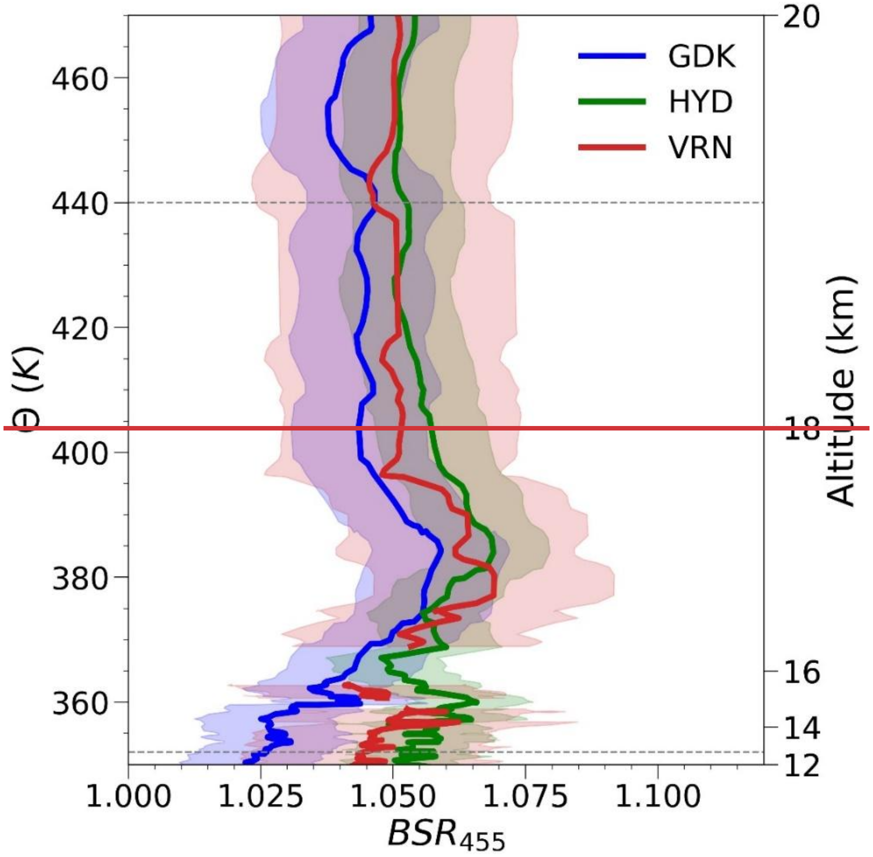

A consistent increase in aerosols is observed in the 16-18 km altitude range (365-400 K potential temperature) across all study locations. The highest BSR455 values are recorded over Varanasi and Hyderabad (~1.07), followed by Gadanki (~1.06), with site-specific variations in backscatter profiles. These findings align with previous ATAL aerosol observations reported by Akhil Raj et al. (2022). The maximum BSR_{455} value (1.07 over Varanasi) is comparable to that observed over Nainital (29.35°N, 79.46°E) in August 2016 (Hanumanthu et al., 2020). For reference, CALIPSO-derived BSR$_{532}$ values for ATAL have been reported to range between 1.10 and 1.15, with an associated depolarization ratio of < 5% (Vernier et al., 2011), further supporting the presence of submicron aerosols in this region.

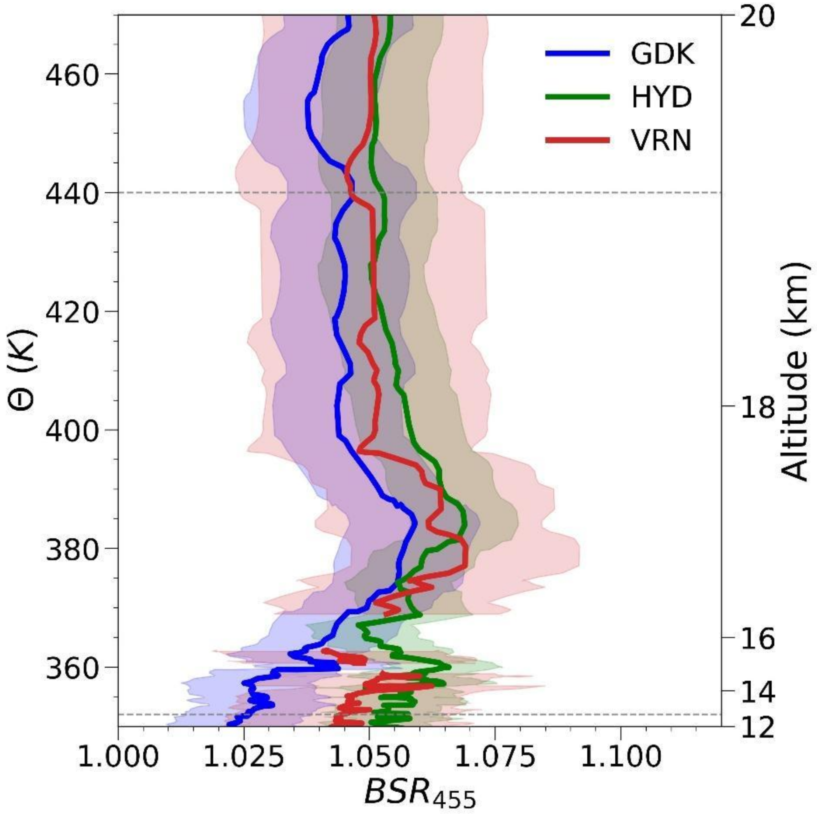

Figure ~~6: The mean~~**4:** Mean cloud-screened backscatter ratios at 455 nm plotted against ~~the~~ potential temperature (Θ) ~~in~~on the primary y-axis and altitude ~~in~~on the secondary y-~~axes~~axis over Gadanki (GDK), Hyderabad (HYD), and Varanasi (VRN). The dashed lines at 13 km and 19 km indicate the ~~typical~~approximate vertical extent of ATAL aerosols~~.~~ (see text for details).

~~An increase in aerosols within this altitude range and potential temperature is evident across all study locations. The BSR~~$_{455}$ ~~peaks at 1.07 over Varanasi and Hyderabad, followed by 1.06 over Gadanki, with slight variations in the pattern of the backscatter profiles at each location. These align with the ATAL aerosol patterns observed previously by Akhil Raj et al. (2022) in these locations. The highest average BSR~~$_{455}$ ~~observed in this study, 1.07 over Varanasi, is comparable to observations over Nainital (29.35° N, 79.46° E) in August 2016 (Hanumanthu et al., 2020). The~~

~~BSR_{532} of ATAL inferred from CALIPSO was between 1.10 and 1.15 on average, with an associated depolarization ratio of less than 5% (Vernier et al. 2011). The enhanced BSR_{455} patterns are more pronounced over Varanasi compared to Hyderabad and Gadanki. Additionally, we observed greater variability in the backscatter over Varanasi, followed by Hyderabad and Gadanki. This is consistent with satellite-based ATAL backscatter measurements, which have shown greater enhancements towards the center of the ASMA region (e.g. Akhil Raj et al., 2022; Vernier et al., 2015). Supporting these findings, the AODs for the UTLS regions, calculated by integrating the extinction profiles derived earlier, indicate that the highest mean AOD_{UTLS} (at 500 nm) occurs at Varanasi and Hyderabad (0.006), followed by Gadanki (0.005). This suggests that the intensity and complexity of ATAL increase as one moves closer to the center of the ATAL region.~~

~~*5.2. Columnar Radiative Forcing Patterns of Sulfate, Nitrate, and Anthropogenic Aerosols in the UTLS:*~~

~~The mean columnar radiative forcing at the TOA, surface (SUR), and within the atmosphere (ATM), estimated for scenarios dominated by sulfate (SUL), nitrate (NIT), and anthropogenic (ANTH) aerosols in the UTLS region (**Fig. 7**).~~

~~The radiative forcing at the TOA (ARF_{TOA}) exhibits a negative sign, indicating a net cooling effect. Among the scenarios, the nitrate-dominated forcing is the most significant, followed by sulfate and anthropogenic aerosols. This outcome is expected, as the predominance of scattering aerosols in the UTLS enhances the reflection of incoming solar radiation back to space, contributing to negative radiative forcing at the TOA.~~

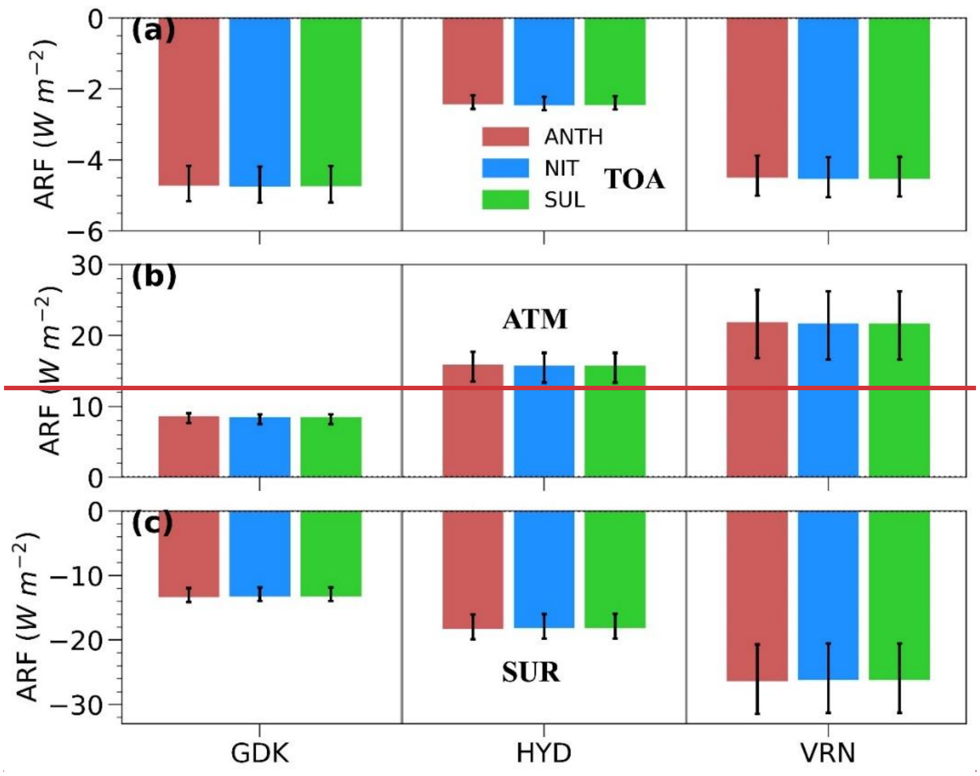

~~**Figure 7:** Aerosol radiative forcing (ARF) estimates at the (a) top of the atmosphere (TOA), (b) column of the atmosphere (ATM), and (c) surface (SUR) estimated with anthropogenic (ANTH), nitrate (NIT), and sulfate (SUL) dominant scenarios in the UTLS across Gadanki (GDK), Hyderabad (HYD), and Varanasi (VRN).~~

~~When analyzing specific locations, we found that ARF$_{TOA}$ estimates are highest over Gadanki, reaching as much as -4.7 ± 0.5 Wm^{-2}, followed closely by Varanasi at -4.5 ± 0.6 Wm^{-2}, with Hyderabad showing significantly lower values at -2.4 ± 0.2 Wm^{-2}. These magnitudes exceed the global average clear-sky aerosol forcing of -1.9 ± 0.3 W m^{-2} reported by Bellouin et al. (2020). Negative aerosol forcing at the TOA has been observed previously across various locations in India under clear-sky conditions. For instance, Santhosh et al. (2024b) reported a forcing -7 ± 0.6 Wm^{-2} at the TOA over Gadanki during the monsoon season, using the long-term CALIPSO aerosol vertical profiles (2006 to 2020). In Hyderabad, previous studies have reported the aerosol radiative forcing ranging from -1 to 7 Wm^{-2} (Gadhavi and Jayaraman, 2006) or as low as -12 Wm^{-2} during~~

~~the early monsoon season (Sinha et al., 2013). On a regional scale, the forcing values observed over Gadanki and Hyderabad in this study are lower than the mean values reported by Kalluri et al. (2020) over Anantapur (14.62° N, 77.65° E), where the mean radiative forcing at the TOA was -6.63 ± 0.77 Wm^{-2}. Over Varanasi, our estimates are comparable to those reported by Vaishya et al. (2018) from the South West Asian Aerosol Monsoon Interactions (SWAAMI) – Regional Aerosol Warming Experiment (RAWEX) campaign, where they estimated a TOA forcing of -6.5 Wm^{-2} during the onset of the monsoon. However, our estimates are lower than those of Subba et al. (2022), who found a TOA forcing of -13 ± 1 Wm^{-2} over Varanasi during the monsoon season using a network of aerosol observatories (ARFINET) combined with concurrent satellite (CERES)-based TOA fluxes.~~

~~The surface forcing across our study locations is also negative. Notably, the anthropogenic scenario in the UTLS region exhibited the largest magnitudes, followed by nitrate, with sulfate showing the lowest values. The highest surface forcing was observed over Varanasi at -26 ± 5 Wm^{-2}, followed by Hyderabad at -18 ± 2 Wm^{-2} and Gadanki at -13 ± 1 Wm^{-2}. The forcing over Gadanki is consistent with the estimate by Santhosh et al. (2024b) of -16.55 ± 0.64 Wm^{-2}, while the observed forcing over Hyderabad is lower than the estimates found by Sinha et al. (2013), where they recorded a forcing of approximately -40 Wm^{-2} in August using ground-based measurements. The surface forcing over Varanasi from our estimates closely matches those of Subba et al. (2022) at -28 ± 2 Wm^{-2} and Vaishya et al. (2018) at -22.9 Wm^{-2}.~~

~~Several factors likely contribute to the varying magnitudes of forcing across the locations. As mentioned earlier, Hyderabad and Varanasi, being heavily urbanized, have a significant presence of absorbing aerosols within the boundary layer. The highest surface forcing in Varanasi, followed by Hyderabad, suggests that these absorbing aerosols reduce the amount of solar~~

~~radiation reaching the surface by absorbing it, leading to localized cooling with greater intensity compared to the rural background location of Gadanki. Complimenting this observation, we identified atmospheric warming or positive forcing within the atmosphere (ATM), with the highest ATM forcing recorded over Varanasi at 21.62 ± 4.8 Wm-2, followed by Hyderabad at 15.6 ± 2.11 Wm^{-2} and Gadanki at 8.35 ± 1 Wm^{-2}. In this case, the anthropogenic aerosol scenario produced the highest forcing, while the sulfate and nitrate estimates were comparable in magnitude. This suggests that the re-emitted thermal energy from the absorbing aerosols is redistributed within the atmospheric column, contributing to warming. The atmospheric forcing over Gadanki and Hyderabad is lower than the estimate of Santhosh et al. (2024b) (13.85 ± 0.35) and Sinha et al. (2013) (20 Wm^{-2}), respectively. In contrast, our estimates of atmospheric forcing for Varanasi are higher than those reported by Subba et al. (2022) (15 ± 1 Wm^{-2}) and Vaishya et al. (2018) (16.4 Wm^{-2}).~~

~~***5.3. Influence of UTLS aerosols and their composition on the total columnar radiative forcing***~~

~~To assess the changes in radiative forcing attributable to UTLS aerosols, particularly in terms of their composition, we analyzed the differences in the radiative forcing between scenarios dominated by absorbing aerosols (ANTH) and scattering aerosols (NIT) relative to a sulfate-dominant (SUL) baseline. The difference in aerosol radiative forcing (ΔARF) was calculated as follows:~~

~~ΔARF_x =~~Despite the observed enhancements, no clear monotonic trend in aerosol concentration emerges across the study locations, which are positioned at different geographical points relative to the ATAL core: Gadanki (southern periphery), Hyderabad (transition region), and Varanasi (central ATAL region). However, the slightly lower aerosol BSR at Gadanki suggests a weaker ATAL influence at the outermost edge. Further validation through extensive in-situ and satellite-based observations is necessary to confirm these spatial trends and understand the seasonal and inter-annual variability of ATAL aerosols.

~~$ARF_x - ARF_{SUL}$ (16)~~

~~where x represents either the ANTH or NIT scenario. These ΔARF values highlight the influence of UTLS aerosols on total columnar radiative forcing.~~

~~Our findings indicate that absorption-dominant UTLS aerosols (ANTH) result in positive radiative forcing at the TOA, while scattering-dominant aerosols (NIT) contribute to a net cooling effect. This is evident from the positive ΔARF values for ANTH at the TOA and the negative value for NIT. The magnitude of these differences is greater in the ANTH scenario than in the NIT scenario, with ΔARF for ANTH reaching up to 0.03 Wm~~$^{-2}$ ~~over Varanasi, followed by 0.02 Wm~~$^{-2}$ ~~over Hyderabad and Gadanki. In contrast, the ΔARF for NIT is -0.015 Wm~~$^{-2}$ ~~across all locations, indicating that the range of radiative forcing at the TOA varies from -0.015 to 0.03 Wm~~$^{-2}$ ~~due to different aerosol scenarios (**Fig.8**).~~

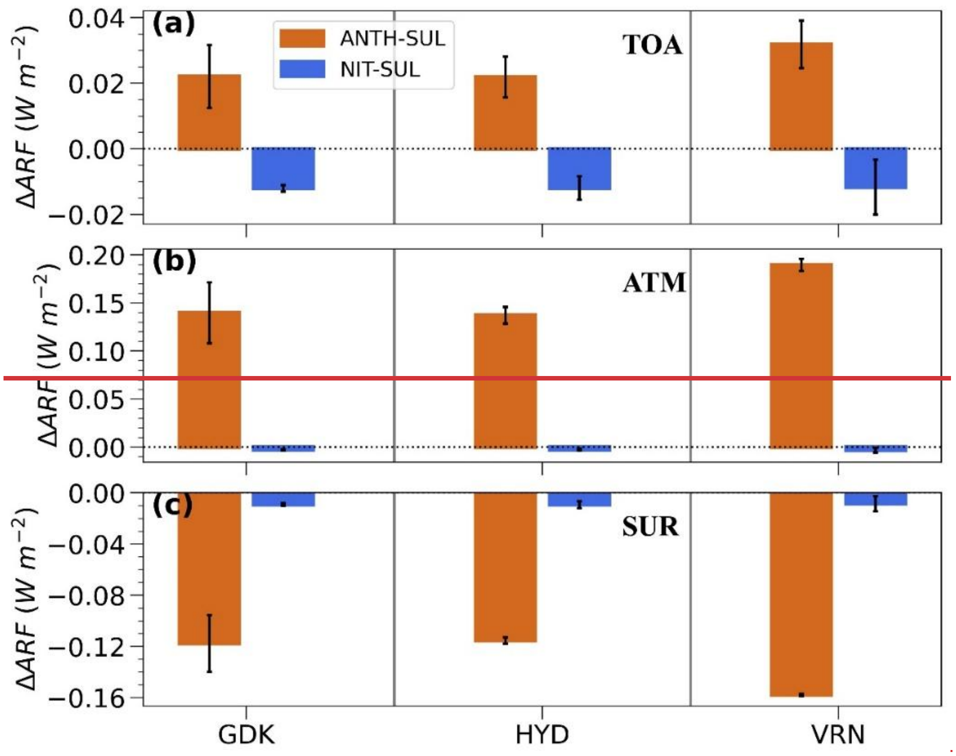

~~**Figure 8**: The differences in the radiative forcing (ΔARF) due to the anthropogenic (ANTH) and nitrate (NIT) compositions with respect to sulfate composition at a) Top of the Atmosphere (TOA), (b) Column of the Atmosphere (ATM), and (c) at the surface (SUR)~~

~~Our estimates are lower than previous studies, such as Vernier et al. (2015), who reported a clear-sky radiative forcing of -0.12 Wm^{-2} at the TOA for ATAL aerosols, comparable to the global radiative forcing from increased CO_2 (0.3 Wm^{-2}). Gao et al. (2023) reported a positive forcing of 0.15 Wm^{-2} using the MERRA-2 reanalysis aerosol product. However, they also observed that the ATAL's impact on TOA forcing varied between -0.002 to 0.15 Wm^{-2} when comparing different reanalysis and forecast products. These variations underscore the significant influence of aerosol composition and measurement methodologies on the estimated radiative forcing. While Vernier et al. (2015) focused on organic carbon and sulfate aerosols, Gao et al. (2023) included black carbon, which increased atmospheric absorption and, consequently, positive~~

~~TOA forcing. In our study, the lower magnitudes, especially in the ANTH scenario, are due to minimizing the aerosol absorption component (**Sect. 4**).~~

~~Interestingly, our findings align more closely with radiative forcing estimates associated with stratospheric and minor volcanic aerosols. For example, the stratospheric aerosol changes since 2000 have been estimated at −0.1 Wm^{-2} using near-global satellite aerosol data, offsetting global warming (Solomon et al., 2011). Similarly, Schmidt et al. (2018) reported a global multiannual mean forcing of −0.08 Wm^{-2} due to frequent small-to-moderate volcanic eruptions between 2005 and 2015, relative to the volcanically quiescent period of 1999–2002. Kloss et al. (2021) documented forcing values ranging from −0.09 ± 0.03 Wm^{-2} to −0.13 ± 0.02 Wm^{-2} due to the Ulawun eruptions in 2019. Although these studies used aerosol extinction profiles in their radiative transfer calculations, assumptions about SSA (from 1.0 to 0.97) and ASY (0.5 to 0.85) were necessary, affecting the results.~~

~~In terms of surface radiative forcing (ΔARF$_{SUR}$), our analysis shows that both ANTH and NIT scenarios contribute to surface cooling, with the ANTH scenario having a more substantial impact. Varanasi exhibited the highest ΔARF$_{SUR,\ ANTH}$ (−0.16 ± 0.001 Wm^{-2}), followed by Hyderabad and Gadanki (−0.12 ± 0.002 Wm^{-2} and −0.12 ± 0.02 Wm^{-2}, respectively). For ΔARF$_{SUR,\ NIT}$, the impact was consistent across locations (−0.01 Wm^{-2}), about one-tenth of the impact from the ANTH scenario. The overall range of surface forcing due to UTLS aerosols, from −0.01 Wm^{-2} to −0.16 Wm^{-2}, though seemingly minor on a local scale, is significant when expressed as −2 Wm^{-2} to −32 Wm^{-2} per unit AOD (at 500 nm). This implies that even small increases in UTLS aerosol loading can substantially enhance surface cooling over time.~~

~~In the atmospheric column (ΔARF_{ATM}), ANTH aerosols were found to enhance atmospheric warming, whereas NIT aerosols contributed to atmospheric cooling. As with TOA forcing, the differences were more pronounced in the ANTH scenario. The highest $\Delta ARF_{ATM, ANTH}$ was observed over Varanasi (0.19 ± 0.001 Wm^{-2}), followed by Hyderabad and Gadanki (0.14 ± 0.01 Wm^{-2} and 0.14 ± 0.03 Wm^{-2}, respectively). Interestingly, $\Delta ARF_{ATM, NIT}$ was negligible (-0.003 Wm^{-2}) across all locations, indicating that the influence of NIT-dominant UTLS aerosols in the atmospheric column is nearly indistinguishable from that of the background sulfate aerosols. This negligible difference can be attributed to the similar SSA values associated with nitrates and sulfates, as noted by Zhang et al. (2012). In this study, the SSA of the UTLS region remained at 1 across both wavelengths (455 nm and 940 nm) (**Fig. 4**), suggesting that any differences in atmospheric forcing estimates between sulfates and nitrates are likely due to slight variations in the column ASY of the UTLS region. In the case of Gadanki, the column asymmetry parameter (ASY) for the UTLS at 455 nm (940 nm) with sulfate aerosols (SUL) is recorded at 0.76 (0.72), whereas for nitrate aerosols (NIT), it is 0.74 (0.70). This has led to the application of sulfate aerosol properties in the estimation of the radiative impacts of nitrates, a method previously employed by various researchers. However, it is important to note that there are significant differences in the single scattering albedo (SSA) between nitrates and sulfates at specific wavelengths. For instance, at a wavelength of approximately 2.8 μm and relative humidity (RH) below 40%, the SSA for nitrates is about 40% higher than that for sulfates (Zhang et al., 2012). This indicates that nitrate aerosols could be more absorptive at these wavelengths, leading to considerable radiative impacts in the UTLS nitrate aerosol column. Since we lack direct measurements at these wavelengths, the radiative impacts of sulfate and nitrate aerosols in the atmospheric column may appear similar.~~

~~However, this similarity should not be interpreted as a justification for substituting the optical and microphysical properties of nitrate aerosols with those of background sulfate aerosols.~~

5.2.~~*5.4.*~~ Impact of UTLS Aerosol Composition on Radiative Forcing ~~*across*~~and its Contribution to the Atmospheric ~~*Layers*~~Column

Figure 5(a) illustrates the ARF in the UTLS region, which exhibits a net positive forcing (warming) across all aerosol combinations. However, under sulfate- and nitrate-dominant scenarios (SUL and NIT, respectively), the warming effect is negligible (<0.02 W m^{-2}) across all locations. In contrast, mixed aerosol scenarios (C1–C5) display a stronger UTLS forcing, ranging from 0.06 to 0.23 W m^{-2} over Gadanki, 0.06 to 0.29 W m^{-2} over Hyderabad, and 0.07 to 0.29 W m^{-2} over Varanasi. Similar magnitudes are observed in Hyderabad and Varanasi, with slightly lower values over Gadanki, indicating a spatial variability in UTLS absorption. Among the mixed aerosol scenarios, the OC-dominant case (C1) exhibits the highest UTLS absorption, whereas C5, where organic carbon (OC) contributes only 10% and ammonium and nitrate dominate (70%), shows the lowest absorption. The successive decrease in UTLS absorption from C1 to C5 highlights the role of absorbing aerosols in enhancing radiative warming in the UTLS. Considering the estimates using previously reported aerosol compositions (C1 from Bossolasco et al., 2021 and C2 from Appel et al., 2022), the UTLS forcing ranged from 0.19 to 0.29 W m^{-2} across different locations.

When considering the total aerosol radiative forcing (ARF$_{ATM}$), the highest values are observed over Varanasi (up to 22.5 W m^{-2}), followed by Hyderabad (up to 16.4 W m^{-2}) and Gadanki (up to 8.92 W m^{-2}) (**Fig. 5(b)**). Since these forcing results from aerosols across multiple atmospheric layers, the UTLS contribution is quantified in terms of the percent fraction of the total ARF (**Fig.**

5(c)). The OC-dominant scenario (C1) exhibits the highest relative UTLS contribution (up to 2.7%), with a decreasing trend as the OC fraction is reduced (C2–C5), consistent with the ARF$_{UTLS}$ variations discussed earlier. In sulfate- and nitrate-dominant cases (SUL and NIT), the UTLS contribution is minimal (0.1%).

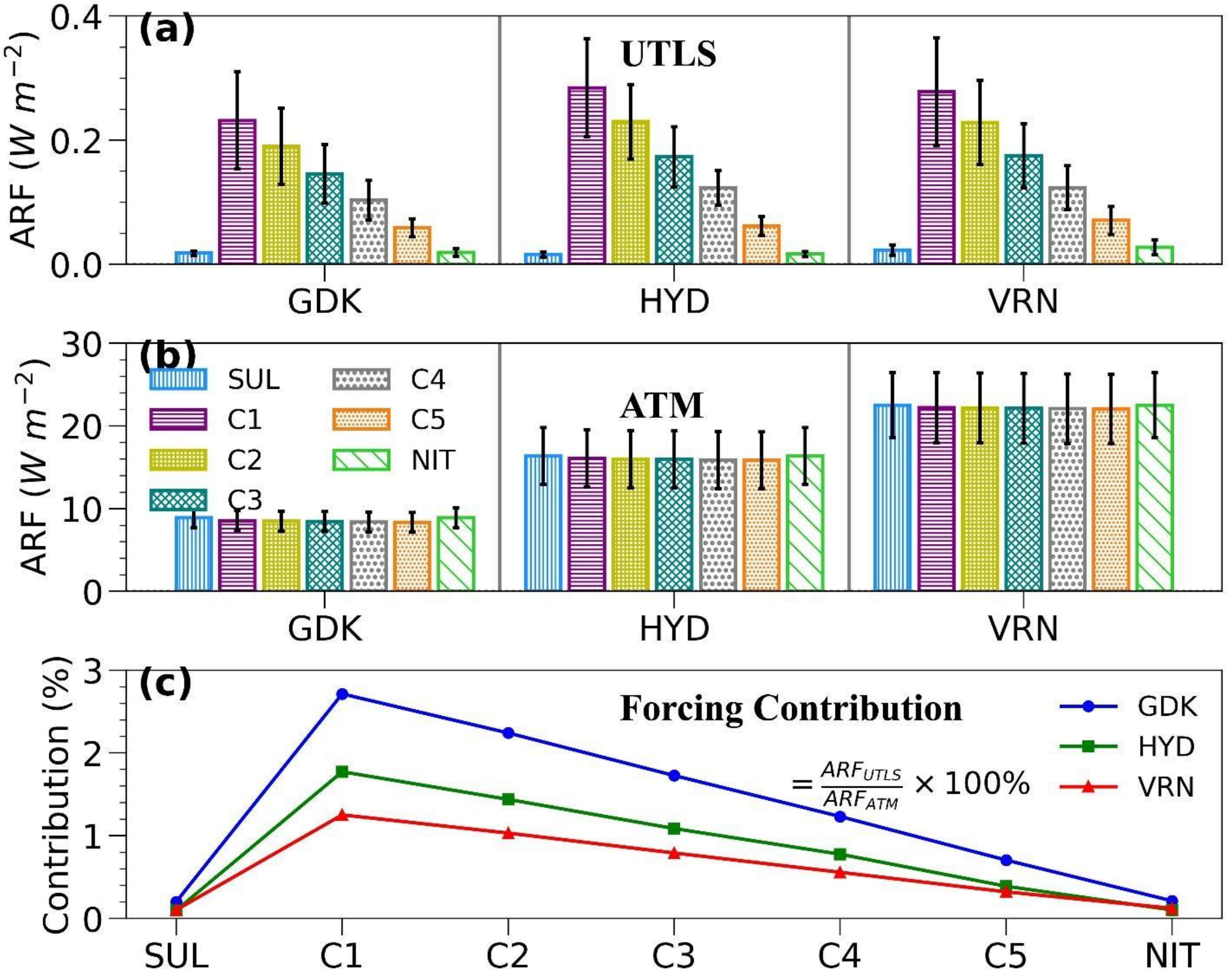

Figure 5: Aerosol Radiative Forcing (ARF) for different aerosol scenarios in the UTLS region over Gadanki (GDK), Hyderabad (HYD), and Varanasi (VRN) during the study period: (a) ARF in the UTLS region, (b) ARF in the total atmospheric column from the surface to 30 km, and (c) percent fractional contribution of UTLS forcing to the total atmospheric forcing.

The variation in UTLS forcing contribution across study locations suggests differences in the overall aerosol distribution within the atmospheric column. Despite similar absolute UTLS forcing values, its relative contribution is highest over Gadanki, moderate over Hyderabad, and lowest over Varanasi. This pattern suggests that over Varanasi, the dominant contribution to atmospheric absorption comes from aerosols in the lower atmosphere, likely driven by the presence of strongly absorbing aerosols in this location (**Table S3**). Conversely, at Gadanki, the lower atmosphere appears to be dominated by scattering aerosols, resulting in reduced absorption, which increases the relative importance of UTLS forcing. These findings underscore the significant impact of lower atmospheric aerosol composition on the contribution of UTLS aerosols to total atmospheric forcing at various locations.

To quantify the influence of aerosol composition on radiative forcing in the UTLS, we examined the difference in radiative forcing (δARF) between various aerosol scenarios and a sulfate-dominant (SUL) reference case. The δARF was computed as:

$$\delta ARF_x = ARF_x - ARF_{SUL}$$

~~The contribution of aerosol radiative forcing within different atmospheric layers - the boundary layer (0 to 2 km), the free troposphere (2 to 12 km), and UTLS (12 to 20 km) - to the total columnar aerosol radiative forcing was evaluated for three different aerosol compositions (**Fig. 9**).~~

~~Our analysis revealed that the ANTH dominant scenario exhibited the highest radiative forcing values within the UTLS, with the greatest magnitude over Varanasi (0.25 ± 0.09 Wm^{-2}), followed by Hyderabad (0.22 ± 0.02 Wm^{-2}) and Gadanki (0.2 ± 0.08 Wm^{-2}). In contrast, the NIT scenario showed much lower forcing values in the UTLS, with 0.02 Wm^{-2} over Gadanki and Hyderabad and a slightly higher value of 0.03 Wm^{-2} at Varanasi. This suggests that the presence of absorbing aerosols in the UTLS leads to localized warming, whereas scattering aerosols contribute to minimal or negligible warming. In terms of percentage contribution to the total~~

~~columnar atmospheric forcing, the UTLS contributes between 0.1% and 2.3% across all locations. Consistent with previous findings, the ANTH dominant scenario in the UTLS contributes the most (1.4% to 2.3%), while the contributions from the NIT and SUL scenarios are significantly lower (0.1% to 0.2%).~~

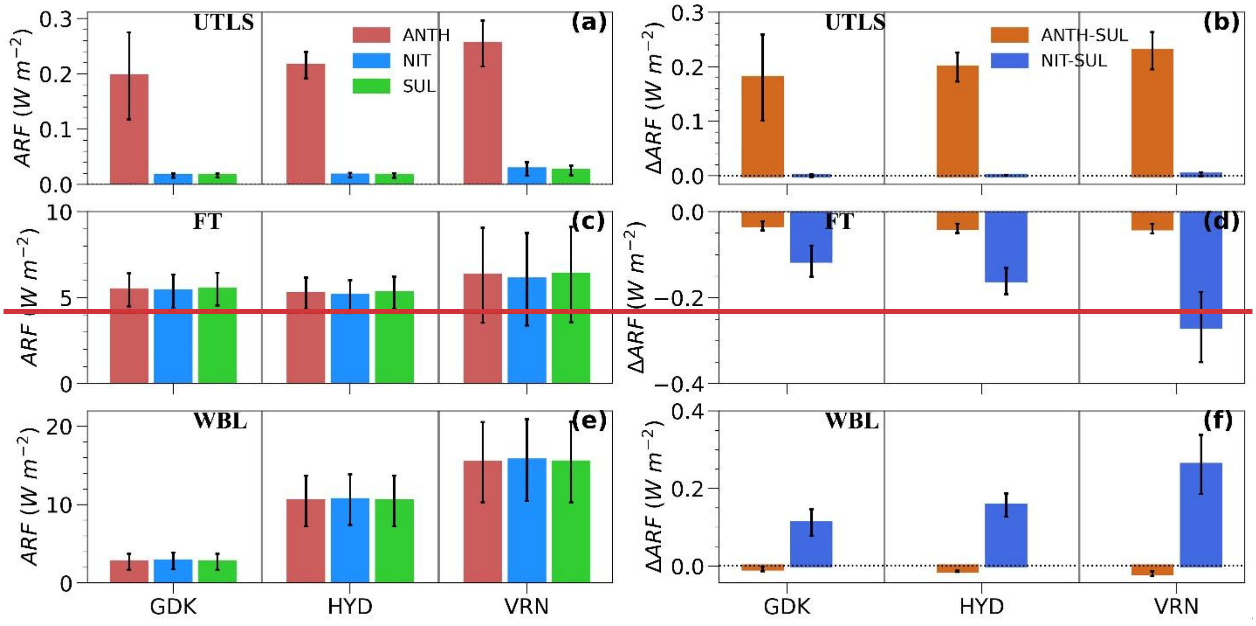

~~**Figure 9:** The contribution of (a) UTLS, (b) Free Troposphere (FT), and (c) Within the boundary layer (WBL) forcing towards the total columnar atmospheric forcing. The right panel (b, d, and f) shows the ΔARF due to ANTH and NIT scenarios with respect to the SUL at UTLS, free troposphere, and within the boundary layer, respectively.~~

~~The right panels of **Fig. 9 (b, d, f)** illustrate the changes in radiative forcing within the boundary layer, free troposphere, and UTLS when transitioning from SUL to either the ANTH or NIT scenarios (ΔARF). Overall, ΔARF values were highest over Varanasi, followed by Hyderabad and Gadanki. Under the ANTH conditions, a slight decrease in radiative forcing was observed in the boundary layer and free troposphere (up to -0.02 Wm^{-2} in the boundary layer and -0.04 Wm^{-2} in the free troposphere). In the UTLS, the transition from SUL to ANTH resulted in a significant increase in radiative forcing, whereas the change from SUL to NIT was minor or negligible. These~~

~~observations suggest that ANTH aerosols in the UTLS absorb incoming solar radiation, leading to localized heating in that layer. This absorption reduces the amount of solar radiation reaching the free troposphere and boundary layer.~~

~~The complex interactions between scattering and absorbing aerosols in the free troposphere further reduce the amount of radiation reaching the boundary layer, eventually leading to decreased radiative forcing within the boundary layer. The ΔARF_{ANTH} per unit AOD of the UTLS (at 500 nm) ranged from -2 to -4 Wm^{-2} in the boundary layer and free troposphere. These changes in the anthropogenic aerosol loading in the UTLS could have a non-negligible long-term impact on the dynamics of the boundary layer and free tropospheric aerosols.~~

~~The similarity in radiative forcing estimates between the SUL and NIT scenarios in the UTLS can be attributed to their similar scattering properties, as discussed earlier. However, ΔARF_{NIT} was found to be positive in the boundary layer and negative in the free troposphere. This is intriguing because it suggests that scattering-dominant aerosols in the UTLS slightly warm the boundary layer while cooling the free troposphere. The scattering effect of nitrates in the UTLS might redistribute solar energy, causing more energy to be scattered and absorbed in the free troposphere, thereby increasing local radiative forcing. In comparison, the boundary layer receives less energy, leading to a reduction in forcing.~~

~~Another possibility is that increased scattering in the UTLS counteracts warming in that layer, stabilizing the atmosphere and reducing vertical mixing. This stabilization could isolate the free troposphere, allowing it to retain more of the scattered energy from the lower atmosphere, thereby increasing local radiative forcing. Consequently, the reduced radiant energy reaching the boundary layer leads to the observed cooling effect.~~

~~It is also important to note that apart from the ATAL, numerous studies have reported the presence of elevated aerosol layers (EALs) in the free troposphere during the pre-monsoon and monsoon months over the Indian region due to long-range transport and vertical convective lofting of aerosols (Kumar et al., 2023; Gupta et al., 2021; Niranjan et al., 2007; Ratnam et al., 2018; Sarangi et al., 2016). These EALs lead to significant radiative impacts, including lower tropospheric cooling due to increased aerosol absorption and scattering, which affects the regional climate and atmospheric stability. Such impacts due to EALs during monsoon months also contribute to the varied influence of the UTLS aerosols in the boundary layer and free troposphere.~~

~~***5.5. Aerosol Heating Rates and their Implications in the UTLS Region***~~

~~Consistent with earlier observations of radiative forcing in this study, heating rates associated with the ANTH~~ (13)

where *x* represents the mixed-aerosol compositions (C1 to C5) and nitrate-dominant (NIT) composition. The sign of δARF_x indicates whether a given aerosol composition induces further warming or cooling in the UTLS and the atmospheric column relative to the sulfate baseline.

In the UTLS, δARF_x values are predominantly positive, suggesting that all tested aerosol compositions—except the nitrate-dominant (NIT) case—contribute to warming (**Fig. 6a**). The δARF for the NIT scenario remains close to zero across all locations, implying minimal radiative influence from nitrate aerosols in the UTLS. The magnitude of δARF_x varies significantly, ranging from 0.06 to 0.28 W m^{-2} (an increase of 300–1400%) over Varanasi, 0.05 to 0.27 W m^{-2} (250–1300%) over Hyderabad, and 0.03 to 0.2 W m^{-2} (150–1000%) over Gadanki. These large variations highlight the strong sensitivity of UTLS radiative forcing to aerosol composition, where even small changes in aerosol properties result in disproportionately large changes in forcing.

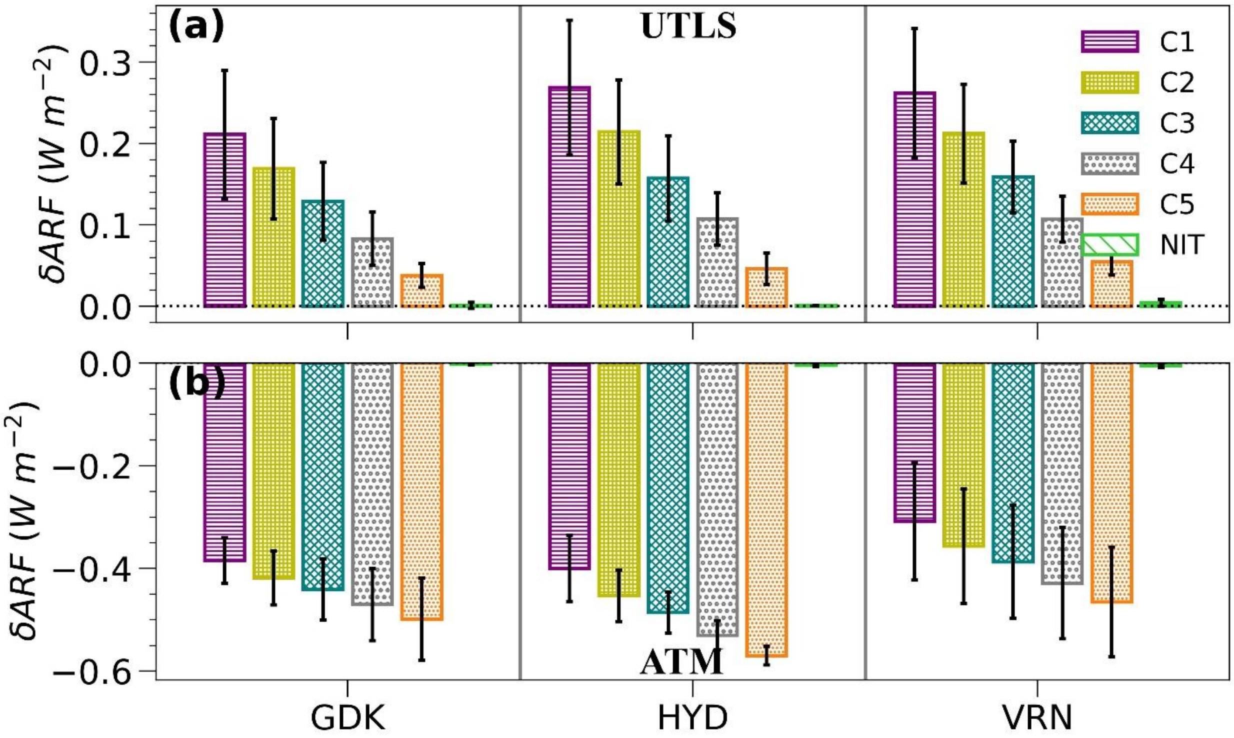

Figure 6: Differences in Aerosol Radiative Forcing (δARF) due to changes in aerosol composition within the UTLS region, with sulfate forcing as the reference (δARF$_x$ = ARF$_x$ – ARF$_{SUL}$, where ‘x’ represents NIT and C1 to C5): (a) δARF in the UTLS region and (b) δARF for the entire atmospheric column.

Among the mixed compositions (C1-C5), the largest δARFx occurs in the OC-dominant scenario (C1) (Bossolasco et al., 2021), highlighting the strong absorptive nature of organic carbon in the UTLS. A progressive reduction in δARF is observed with decreasing OC fraction and increasing nitrate and ammonium content (C2 to C5), indicating that absorbing aerosols, such as OC, substantially modify the UTLS radiative forcing. In the atmospheric column, δARF$_{ATM}$ values are negative, indicating that changes in UTLS aerosol composition led to a decrease in atmospheric forcing (**Fig. 6b**). The magnitudes of δARF$_{ATM}$ reach approximately -0.5 W m^{-2} (5%) over Gadanki, -0.6 W m^{-2} (4%) over Hyderabad, and -0.5 W m^{-2} (2.3%) over Varanasi. This suggests that while UTLS aerosol composition significantly alters radiative forcing at high altitudes, the net effect on the entire atmospheric column remains relatively modest.

5.3. Influence of Aerosol Composition on Heating Rates in the UTLS

Shortwave heating rates associated with mixed-type aerosol compositions in the UTLS (C1 to C5) are significantly higher than those observed ~~in the~~ under sulfate- (SUL) and nitrate-dominant (NIT) scenarios (**Fig.** ~~**10**). Specifically, the heating rates in the SUL and NIT scenarios are nearly 10 times smaller than those in the ANTH dominant scenario.~~7). Neither the SUL nor NIT ~~scenarios displayed~~cases exhibit distinct heating rate patterns at ~~the~~ ATAL altitudes, with only slight warming observed, ~~reaching a maximum of~~peaking at approximately 0.003 K day^{-1}. This ~~lack of~~negligible difference ~~in heating rate patterns~~ between sulfate and nitrate aerosols can be attributed to their similar optical properties, as discussed in ~~previous sections.~~

Santhosh et al. (2025). In contrast, ~~under the ANTH composition,~~ enhanced heating rates ~~were~~are observed ~~from~~between 16~~ km to ~~–18 km~~ over Gadanki~~ (365~~ to ~~–404 K potential temperature~~), from 14km to~~) over Gadanki, 14–16 km (357~~ to ~~–366 K~~ potential temperature~~) over Hyderabad, and ~~from~~ 16~~ km to ~~–18 km (367~~ to ~~–403 K~~ potential temperature~~) over Varanasi~~. This for the mixed aerosol scenarios (C1 to C5). The~~ heating in the ATAL layer ~~reached as high as~~reaches a maximum of 0.03 K day^{-1}, ~~indicating a slight warming due to the presence of absorbing aerosols in the UTLS region. The heating rates over Varanasi were~~with Varanasi exhibiting notably higher heating rates than ~~those at~~ the other locations.

Consistent with the discussion on UTLS radiative forcing, the highest heating rates occur in the OC-dominant composition (C1). A progressive decline is observed as the OC fraction decreases while ammonium and nitrate fractions increase (C2 to C5). These results highlight the warming effect of absorbing aerosols in the UTLS. Previous studies~~ support these findings; for instance,~~ , such as Fadnavis et al. (2022~~)~~), reported UTLS warming due to anthropogenic aerosols, with estimates ranging from 0.02 to 0.3 K per month~~.~~, equivalent to an upper limit of ~0.01 K day^{-1}. Similarly, carbonaceous aerosols~~, which have~~ with strong absorption characteristics~~,~~ ~~increased~~ have been shown to increase UTLS heating by 0.001 to 0.02 K day^{-1} (Chavan et al., 2021).

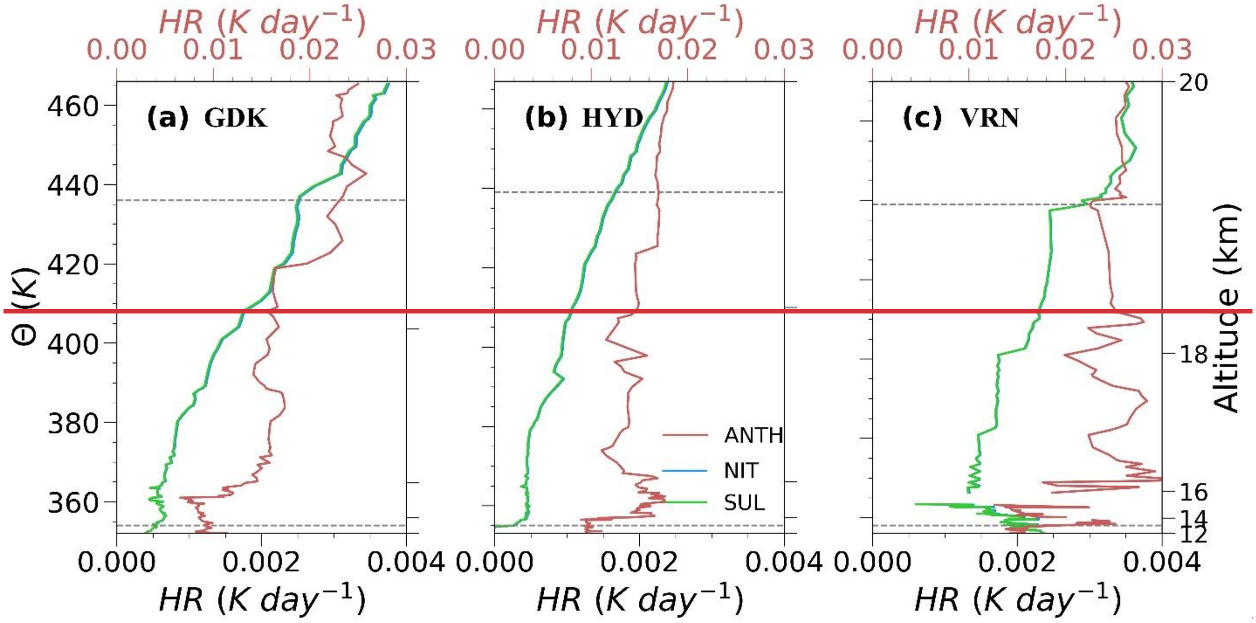

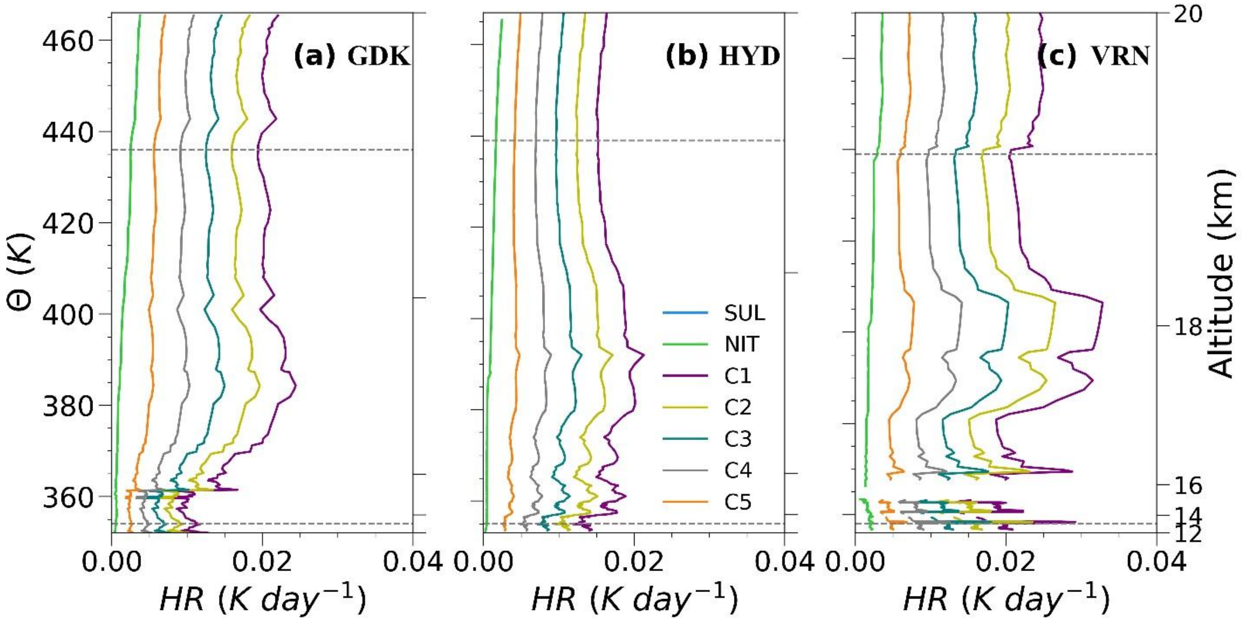

Figure ~~10: The aerosol~~7: Aerosol heating rates ~~at~~in the UTLS plotted against potential temperature (Θ) and altitude over (a) Gadanki, (b) Hyderabad, and (c) Varanasi. The ~~grey~~gray dashed lines at 13 km and 19 km ~~represent~~indicate the approximate vertical extent of ATAL.

~~This warming in the UTLS region could have several significant consequences. As warming occurs in the boundary layer and free troposphere, the elevated temperature in the UTLS could lead to an increase in water vapor concentration in the lower stratosphere. Fadnavis et al. (2022) noted that South Asian aerosols contribute to enhanced water vapor levels in the lower stratosphere at tropical and subtropical latitudes. As a potent greenhouse gas, increased water vapor in the UTLS region could amplify warming through positive feedback mechanisms. Huang et al. (2016) estimated a weak positive global-mean radiative feedback (0.02 ± 0.01 W m^{-2} K^{-1}) due to increased stratospheric water vapor concentration. Furthermore, Solomon et al. (2010) estimated that a 1 ppmv increase in water vapor could lead to a global average radiative forcing of 0.24 W m^{-2} at the TOA, comparable to the 0.36 W m^{-2} increase in radiative forcing due to the growth of carbon dioxide from 1980 to 1996.~~

~~Another potential consequence of increased water vapor in the lower stratosphere is ozone depletion. For example, box-model simulations by Robrecht et al. (2019) showed that high water vapor mixing ratios could lead to approximately 20% of ozone destruction through catalytic ozone loss cycles. In addition, UTLS warming and associated increases in water vapor could influence aerosol microphysical properties. Balloon-borne measurements by He et al. (2019) revealed that larger particles in the UTLS aerosol layer, which are generally very hydrophilic, experience dramatic size increases with rising relative humidity. These size changes can further alter the scattering and absorption characteristics of aerosols, leading to varied radiative impacts. Consequently, the dominant presence of absorbing aerosols in the UTLS has the potential to create a complex feedback mechanism, influencing the radiative balance by altering the compositions of water vapor, ozone, aerosols, and trace gases.~~

~~6.~~ To evaluate the sensitivity of heating rates to changes in aerosol composition within the ATAL region, we estimate the difference in heating rates (δHR) for the nitrate (NIT) and mixed-aerosol compositions (C1–C5) relative to the sulfate (SUL) reference scenario across 13–19 km as:

$$\delta HR_x = HR_x - HR_{SUL} \qquad (14)$$

where *x* represents aerosol compositions other than sulfates. The δHR values range from ~0 to 0.03 K day^{-1} across the locations (**Fig. 8**).

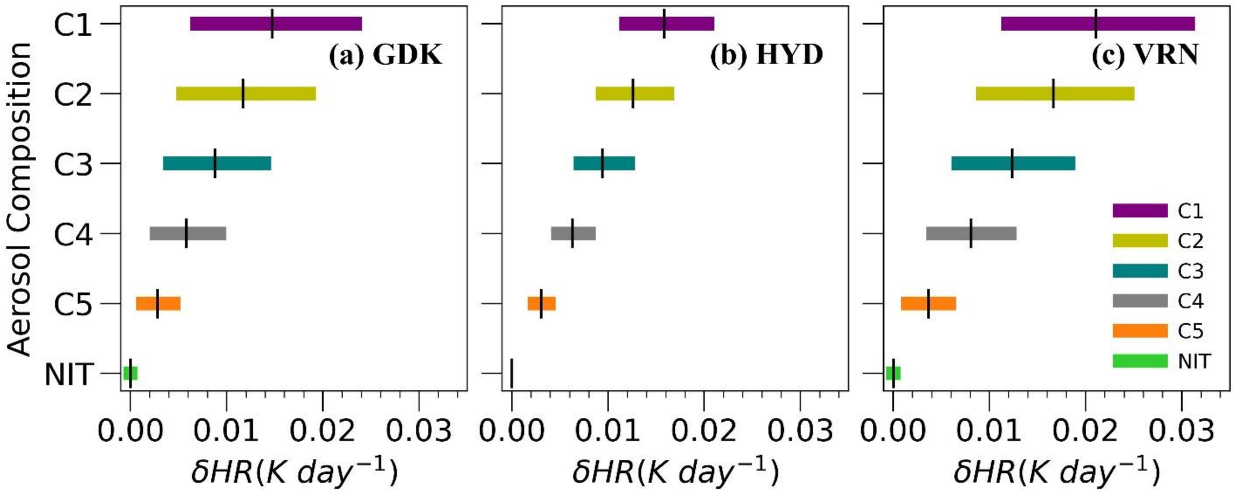

Figure 8: Range of changes in aerosol heating rates due to different aerosol compositions relative to the sulfate-dominant scenario (δHR = HR_x - HR_{SUL}, where 'x' represents compositions other than sulfates) over (a) Gadanki (GDK), (b) Hyderabad (HYD), and (c) Varanasi (VRN). Horizontal bars represent the minimum-to-maximum range of δHR, while small black vertical markers indicate the mean values.

A broader range of δHR is observed for compositions with a higher OC fraction, such as C1 (50% OC) and C2 (40% OC), leading to heating rate increases from 0.01 to 0.03 K day^{-1}, which is approximately 10–30 times larger than the sulfate baseline. As the OC fraction decreases, the δHR range also diminishes, similar to the δARF trend discussed earlier. Due to the comparable heating rates of nitrate and sulfate aerosols in the UTLS, the δHR associated with the NIT scenario remains negligible. However, when nitrates constitute a significant portion of the mixed compositions (e.g., 30% in C5 and 40% in C4), along with ammonium aerosols (40% in C5 and 30% in C4), δHR values become non-negligible (~0.001 to 0.01 K day^{-1}), leading to a 10-fold increase in heating rates compared to the sulfate reference. These results confirm that variations in aerosol composition in the UTLS have a substantial impact on heating rates, further influencing radiative effects and atmospheric stability in this region.

5.4. Comparison of Heating Rates at Point Locations Relative to Spatially Averaged Estimates

Since this study focuses on heating rates at specific point locations, it is valuable to compare these estimates with those obtained for a broader spatial domain using a similar methodology. A recent study by Santhosh et al. (2025) examined radiative forcing and heating rates in the 12–20 km altitude range over a broader geographic region within the Asian Summer Monsoon Anticyclone (ASMA) (25°N–37.5°N, 40°E–95°E) using Cloud-Aerosol Lidar with Orthogonal Polarization (CALIOP) data. In that study, three dominant aerosol scenarios were considered in the UTLS: sulfate, nitrate, and anthropogenic aerosols. The sulfate and nitrate aerosols had microphysical properties similar to those in our study, while the anthropogenic aerosol model was based on the continental clean aerosol model of Hess et al. (1998), representing a mixed-aerosol scenario.

To assess the representativeness of the point-location heating rates, we compare the sulfate- and nitrate-dominated cases from the present study with the corresponding heating rates reported by Santhosh et al. (2025). Although a direct comparison of mixed aerosols is more complex due to differences in aerosol definitions, we use the composition with the highest heating rates from this study (C1) as a reference for comparison against the anthropogenic heating rates reported by Santhosh et al. (2025).

Our analysis reveals that heating rates at individual locations (Gadanki, Hyderabad, and Varanasi) are slightly higher than the spatially averaged heating rates over the ASMA region under sulfate- and nitrate-dominant scenarios (**Fig. 9**). However, for the mixed-aerosol scenarios, the heating rates estimated over the ASMA region exceed those observed at individual point locations.

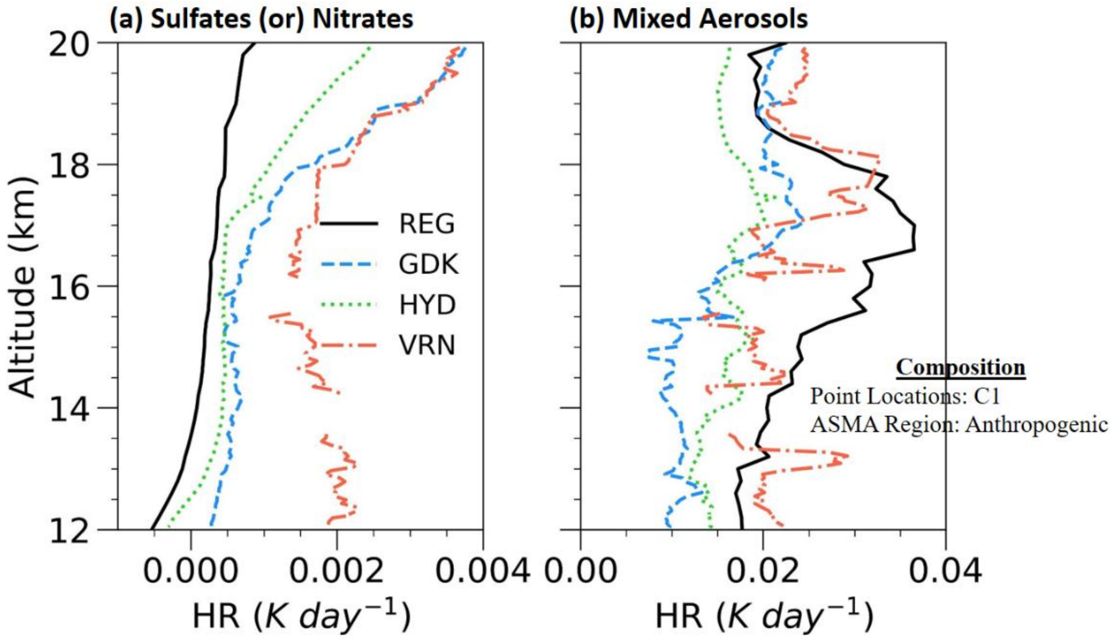

Figure 9: Comparison of UTLS heating rates for (a) sulfate or nitrate-dominant composition and (b) mixed aerosol composition across the UTLS region (REG: 25°N–37.5°N, 40°E–95°E, adapted from Santhosh et al. (2025)), as well as over Gadanki (GDK), Hyderabad (HYD), and Varanasi (VRN). In the mixed aerosol scenario, the composition with the highest observed heating rates (C1) is compared with the anthropogenic composition in the UTLS region reported by Santhosh et al. (2025). As Santhosh et al. (2025) also observed a near-similar heating rate pattern for sulfates and nitrates, consistent with the present study, only heating rates with nitrates are plotted here.

This discrepancy can be attributed to the interplay between aerosol optical properties and spatial averaging effects. Santhosh et al. (2025) assumed that the climatological mean and standard deviation profiles of aerosol backscatter ratios sufficiently capture the spatial heterogeneity of ATAL in radiative transfer calculations. Scattering aerosols, such as sulfates and nitrates, primarily reflect shortwave radiation and do not significantly contribute to global warming or atmospheric heating. When averaged over a large spatial domain, the weak radiative response of these aerosols is integrated across a broader region, leading to lower overall heating rates.

In contrast, the heating effects of absorbing aerosols within mixed-aerosol scenarios are less sensitive to spatial heterogeneity. Even small fractions of absorbing aerosols in the ATAL contribute to warming, and regional averaging enhances this consistent heating effect. This explains why the ASMA-wide mixed-aerosol heating rates exceed those at point locations. These findings suggest that the mixed-aerosol compositions considered in this study may lead to stronger warming in the UTLS over a broader spatial domain. Further investigations with realistic observational constraints and model validation are needed to better quantify these effects.

6. Summary and Conclusions

This study ~~provides~~presents a detailed analysis of the shortwave radiative impacts of monsoon UTLS aerosols, focusing on radiative forcing and heating rates~~, based on~~ derived from balloon-borne in situ measurements ~~from the~~ conducted as part of the Balloon Measurement Campaigns of the Asian Tropopause Aerosol Layer (BATAL~~ field campaigns conducted~~) between 2014 and 2018. To assess ~~the~~ aerosol effects, ~~three idealized scenarios were~~we considered~~, each~~ seven aerosol compositions dominated by ~~a~~ different ~~type of aerosol~~species: (i) ~~Sulfate~~sulfate (SUL~~)~~), representing the background or reference condition, (ii) ~~Nitrate~~nitrate (NIT~~) for~~), a primarily scattering~~ dominant aerosols~~ aerosol, and (iii) ~~Anthropogenic (ANTH) for absorption-dominant aerosols.~~five mixed-type aerosol scenarios incorporating varying fractions of sulfates, nitrates, organic carbon, and ammonium aerosols. The key findings from ~~the~~this study, ~~conducted over three locations~~ based on measurements at Gadanki, Hyderabad, and Varanasi~~–~~, are summarized ~~below~~as follows:

~~i)~~(i) **Aerosol Enhancement in ATAL Altitudes**: A significant ~~increase~~enhancement in aerosol ~~concentrations~~backscatter was observed ~~at~~in the ~~ATAL altitudes (~~13~~ to ~~–19 km~~)~~ altitude range across all locations, with BSR455 peaks reaching ~~as high as~~up to 1.07 over Varanasi and Hyderabad~~, followed by~~ and 1.06 over Gadanki. ~~The highest mean AOD in the UTLS was recorded over Varanasi, followed by Hyderabad and Gadanki, indicating the strength and complexity of ATAL vary from the edge to the center of the ASMA region.~~

~~ii)~~ **UTLS Radiative Forcing** ~~**across Layers**: The study found cooling effects at the top of the atmosphere (TOA) ranging from -2.37 ± 0.19 Wm^{-2} to -4.5 ± 0.6 Wm^{-2}~~ **and** ~~at the surface from -12.9 ± 1 Wm^{-2} to -26 ± 5 Wm^{-2}. At the same time, warming~~ **its contribution to total atmospheric forcing:** A net positive aerosol forcing was observed ~~within the atmospheric column, ranging from 8.21 ± 0.68 Wm^{-2} to 21.62 ± 4.8 Wm^{-2}. The ANTH scenario showed the highest radiative forcing magnitudes~~ in the UTLS~~, nearly comparable with the SUL and NIT scenarios.~~

~~iii) **Changes in Radiative Forcing (ΔARF)**: The influence of UTLS aerosols on radiative forcing at TOA, surface (SUR), and within the atmosphere (ATM) was quantified by comparing the changes from the reference SUL composition to the NIT and ANTH compositions. The ΔARF due to ANTH aerosols was positive (indicating warming) at TOA and ATM but negative (indicating cooling) at the surface. Conversely, ΔARF due to NIT aerosols was negative across TOA, SUR, and ATM. The radiative forcing changes in the~~

~~TOA ranged from -0.015 to 0.03 Wm^{-2}, at the surface from -0.01 Wm^{-2} to -0.16 Wm^{-2}, and within the atmosphere from 0 to 0.19 Wm^{-2}. These changes are similar to the radiative impacts of minor volcanic eruptions and could have long-term effects on regional weather patterns. The most significant impacts were observed over Varanasi, followed by Hyderabad and Gadanki.~~

~~iv)~~(ii) ~~**Contribution of UTLS Aerosols to Total Columnar Forcing**: The UTLS aerosols contributed~~region, contributing between 0.1% and ~~2.~~3% of the total ~~columnar~~ atmospheric column forcing. ~~The ANTH~~Among the tested compositions, the scenario ~~had~~with 50% organic carbon (C1) exhibited the highest contribution (1.~~4% to 2.~~25%–3%), ~~while the NIT~~whereas nitrate- and ~~SUL~~sulfate-dominated scenarios contributed significantly less (0.1~~% to~~ %–0.2%). The highest UTLS forcing estimates ~~in the UTLS column~~ were recorded over Varanasi ~~(~~and Hyderabad (~0.~~25 ± 0.09 Wm^{-2}),~~3 W m^{-2}), followed by ~~Hyderabad (0.22 ± 0.02 Wm^{-2}) and~~ Gadanki (0.~~2 ± 0.08 Wm^{-2}) under the ANTH scenario.~~23 W m^{-2}). Under ~~the NIT scenario, the~~ sulfate- and nitrate-dominant conditions, forcing remained nearly uniform across locations, with values not exceeding 0.02 W m^{-2}. The UTLS forcing ~~values were 0.02 Wm^{-2} over Gadanki and Hyderabad, with a slightly higher value of 0.03 Wm^{-2} over Varanasi~~decreased with increasing fractions of nitrate and ammonium.

~~v) **Impact on Boundary Layer and Free Troposphere**: UTLS aerosols also influenced the radiative balance within the boundary layer (WBL) and free troposphere (FT). Under the ANTH scenario, a slight decrease in radiative forcing (cooling) was observed in the WBL~~

~~and FT (up to -0.04 Wm^{-2}). In contrast, the NIT scenario resulted in a slight increase in the WBL (up to 0.26 Wm^{-2}) and a slight decrease (cooling) in the FT (up to -0.27 Wm^{-2}).~~

~~vi)~~(iii)**Heating ~~Rate Profiles~~Rates in the UTLS Region:** The heating rate profiles for ~~the UTLS under the ANTH scenario showed~~mixed-aerosol compositions exhibited a ~~marked~~notable increase in aerosol-induced heating at ~~the~~ ATAL altitudes, with~~ the highest~~ rates ~~recorded over Varanasi (~~reaching up to 0.03 ~~Kday^{-1}), compared to other~~K day^{-1} across the study locations. However, ~~the~~ heating rates ~~under the SUL~~for sulfate- and ~~NIT~~nitrate-dominant scenarios were ~~nearly~~approximately one-tenth of those ~~under the ANTH scenario, indicating~~observed under mixed-aerosol conditions, suggesting significantly ~~lower~~weaker or negligible heating.

~~Overall, this study demonstrated that ATAL aerosols in the UTLS have diverse impacts on different atmospheric layers, varying across geographic locations within the ATAL region. The scattering and absorption properties of the aerosols present strongly influence these impacts. The actual composition of ATAL is likely complex, given the chemical and dynamic variability within the region (e.g., Hanumanthu et al., 2020). Therefore, altitude-resolved aerosol composition data from real-time measurements are crucial for accurately assessing their radiative impacts, which also applies to aerosols within the boundary layer and free troposphere. It is important to emphasize that the radiative forcing and heating rates of nitrate and sulfate aerosols are comparable within the atmospheric column and UTLS due to their similar scattering properties across a broad range of shortwave spectrum wavelengths. However, to capture the specific absorption characteristics of nitrate aerosols at particular wavelengths, improved measurement techniques in the thermal infrared and longwave regions are needed. Enhancing these measurements will also aid studies on~~

~~UTLS water vapor, a potent greenhouse gas whose radiative impacts are more sensitive in the longwave region (e.g., Santhosh et al., 2024a).~~

(iv) ~~The strength of ATAL backscatter ratios varies geographically within the ASMA region, leading to corresponding variations in radiative forcing and~~**Influence of the UTLS aerosol composition on the radiative forcing and heating rates:** To quantify the impact of aerosol composition on radiative forcing, we used the sulfate-dominant scenario as a reference. While replacing sulfates with nitrates led to minimal changes in radiative forcing, the inclusion of organic carbon and ammonium in mixed-aerosol compositions resulted in disproportionate increases in UTLS radiative forcing (up to 14-fold). However, in terms of total column atmospheric forcing, these changes were relatively modest, with a maximum reduction of ~5%, underscoring the localized nature of UTLS radiative effects. Heating rate variations followed a similar pattern, with mixed-aerosol scenarios exhibiting up to a 30-fold increase compared to sulfate-dominated conditions.

(v) **Comparison with Spatially Averaged UTLS Heating Rates:** When comparing our point-location heating rate estimates with spatially averaged heating rates~~. The highest values were observed over Varanasi, a more centrally located area within the region. In contrast, estimates for Hyderabad and Gadanki, located near the edges of the ATAL region, were comparable. However, further verification of this pattern on a global~~ over the ASMA region (Santhosh et al., 2025), we found that mixed absorbing and scattering aerosols produced a stronger regional warming effect, whereas purely scattering aerosols (e.g., sulfates, nitrates) had a weaker impact. This suggests that regional-scale

~~across the entire ATAL region is necessary.~~ radiative effects are more sensitive to variations in ATAL aerosol composition.

Although this study considered near-realistic aerosol compositions for the ATAL, the actual chemical composition of UTLS aerosols remains a challenge due to spatial and temporal variability (Hanumanthu et al., 2020). Observational datasets with altitude-resolved aerosol composition are essential for improving radiative impact assessments. Additionally, while dust and black carbon have been detected in the ATAL (Bossolasco et al., 2021; Ma et al., 2019), previous studies have shown that dust has minimal impact on clear-sky shortwave heating rates (Gao et al., 2023), and black carbon concentrations are modest in the ATAL, as indicated by recent in situ measurements (Appel et al., 2022; Vernier et al., 2022). Therefore, these species were excluded from our analysis.

A significant limitation of the study is its reliance on shortwave radiative effects, as nitrate and sulfate aerosols exhibit similar scattering properties across the shortwave spectrum. However, nitrates have distinct absorption features in the thermal infrared, which could influence longwave radiative forcing. Future studies should incorporate improved measurements in the longwave and thermal infrared regions to assess the full radiative impact of nitrate aerosols. Additionally, given the sensitivity of UTLS radiative effects to water vapor concentrations (Santhosh et al., 2024a), further investigations are necessary to assess the coupled effects of aerosols and water vapor on the UTLS radiative balance.

Given the geographic and temporal limitations of in-situ ~~measurements,~~observations, an integrated approach combining satellite ~~data~~retrievals, reanalysis~~, and~~ datasets, and in-situ measurements is crucial for tracking long-term trends in~~-situ measurements is essential, and~~ ATAL radiative forcing and heating rates. Ongoing efforts in this direction are ~~currently underway.~~

~~Moreover, a series of experiments as part of the~~ expected to refine our understanding of the effects of UTLS aerosols. One of the key questions that remains unexplored is whether the ATAL aerosol's chemical composition has any role in strengthening or weakening the monsoon anticyclone. By modulating radiative heating, aerosols can influence the temperature gradient and stability of the upper troposphere, potentially altering the strength and persistence of the anticyclonic circulation. Finally, the second phase of ~~the~~ BATAL ~~campaigns, concluded~~, which commenced in August 2024, ~~are expected~~is anticipated to ~~provide~~yield new insights into ATAL ~~research~~composition and radiative effects, particularly regarding the ~~influence~~impact of wildfires and volcanic eruptions. These findings will be instrumental in refining the understanding of UTLS aerosol-radiation interactions.

Code/Data availability

The data collected from the BATAL campaigns is available on request.

Author contribution

V.N. Santhosh: Data curation, Formal analysis, Investigation, Software, Validation, Visualization, Writing – original draft. **B.L. Madhavan:** Conceptualization, Investigation, Methodology, Supervision, Writing – review & editing. **S.T. Akhil Raj:** Data curation, Visualization, Writing – review & editing. **M. Venkat Ratnam:** Supervision, Project administration, Resources, Writing – review & editing. **J-P. Vernier:** Project administration, Resources, Writing – review & editing. **F.G. Wienhold:** Software, Writing – review & editing.

Competing interests

The authors declare that they have no conflict of interest.

Acknowledgements

The findings presented in this paper are derived from the ISRO-NASA joint BATAL campaign, which was supported by the National Atmospheric Research Laboratory (NARL) under the Department of Space (DoS~~),~~) and NASA ROSES Upper Atmospheric Research Program and Atmospheric Composition Modeling and Analysis Program (UARP, ACMAP, UACO). We extend our gratitude and acknowledge Dr. Amit Kumar Pandit, National Institute of Aerospace, Hampton, USA, and other members from NARL Gadanki, TIFR Balloon Facility, Hyderabad, and BHU Varanasi for their active involvement in the BATAL ~~campaigns~~project from Gadanki to Varanasi. We thank NASA's Earthdata team for providing free access to their MERRA-2, MODIS, MLS, and AIRS datasets, which were used as supportive data in this study. We also thank the National Oceanic and Atmospheric Administration (NOAA)'s Air Resources Laboratory (ARL) for their HYSPLIT software.

References

Akhil Raj, S. T., Venkat Ratnam, M., Narayana Rao, D., ~~&~~and Krishna Murthy, B. V~~. (2015).~~.: Vertical distribution of ozone over a tropical station: Seasonal variation and comparison with satellite (MLS, SABER) and ERA-Interim products~~. *Atmospheric Environment, 116*, 281–292. https://doi.org/10.1016/j.atmosenv.2015.06.047~~, Atmos. Environ., 116, 281–292, https://doi.org/10.1016/j.atmosenv.2015.06.047, 2015.

Akhil Raj, S. T., Ratnam, M. V., Vernier, J. P., Pandit, A. K., ~~&~~and Wienhold, F. G~~. (2022).~~.: Defining the upper boundary of the Asian Tropopause Aerosol Layer (ATAL) using the static stability~~. *Atmospheric Pollution Research*,~~, Atmos. Pollut. Res., 13(6), 101451~~.~~, ~~https://doi.org/10.1016/j.apr.2022.101451~~https://doi.org/10.1016/j.apr.2022.101451, 2022.

Angstrom, A~~. (1964).~~.: Technique of determining the turbidity of the atmosphere, Tellus, 13(2), 214-223~~.~~, ~~https://doi.org/10.1111/j.2153-3490.1961.tb00078.x~~https://doi.org/10.1111/j.2153-3490.1961.tb00078.x, 1964.

Appel, O., Köllner, F., Dragoneas, A., Hünig, A., Molleker, S., Schlager, H., Mahnke, C., Weigel, R., Port, M., Schulz, C., Drewnick, F., Vogel, B., Stroh, F., ~~&~~and Borrmann, S~~. (2022).~~.: Chemical analysis of the Asian tropopause aerosol layer (ATAL) with emphasis on secondary aerosol particles using aircraft-based in situ aerosol mass spectrometry~~. *Atmospheric Chemistry and Physics, 22*(20), 13607–13630. https://doi.org/10.5194/acp-22-13607-2022~~, Atmos. Chem. Phys., 22(20), 13607–13630, https://doi.org/10.5194/acp-22-13607-2022, 2022.

Basha, G., Ratnam, M. V., Jiang, J. H., Kishore, P., ~~&~~and Babu, S. R~~. (2021).~~.: Influence of indian summer monsoon on tropopause, trace gases and aerosols in ~~asian~~Asian summer monsoon anticyclone observed by ~~cosmic, mls~~COSMIC, MLS and ~~calipso.~~CALIPSO, Remote ~~*Sensing*,~~Sens., 13(17~~). https://doi.org/10.3390/rs13173486~~), https://doi.org/10.3390/rs13173486, 2021.

~~Bellouin, N., Quaas, J., Gryspeerdt, E., Kinne, S., Stier, P., Watson-Parris, D., Boucher, O., Carslaw, K. S., Christensen, M., Daniau, A. L., Dufresne, J. L., Feingold, G., Fiedler, S., Forster, P., Gettelman, A., Haywood, J. M., Lohmann, U., Malavelle, F., Mauritsen, T., … Stevens, B. (2020). Bounding Global Aerosol Radiative Forcing of Climate Change. *Reviews of Geophysics, 58*(1), 1–45. https://doi.org/10.1029/2019RG000660~~

Bossolasco, A., Jegou, F., Sellitto, P., Berthet, G., Kloss, C., ~~&~~and Legras, B~~. (2021).~~.: Global modeling studies of composition and decadal trends of the Asian Tropopause Aerosol Layer~~. *Atmospheric Chemistry and Physics*,~~, Atmos. Chem. Phys., 21(4), 2745–2764~~. https://doi.org/10.5194/acp-21-2745-2021~~, https://doi.org/10.5194/acp-21-2745-2021, 2021.

Chavan, P., Fadnavis, S., Chakroborty, T., Sioris, C. E., Griessbach, S., ~~&~~and Müller, R~~. (2021).~~.: The outflow of Asian biomass burning carbonaceous aerosol into the upper troposphere and lower stratosphere in spring: Radiative effects seen in a global model~~. *Atmospheric Chemistry and Physics, 21*(18), 14371–14384. https://doi.org/10.5194/acp-21-14371-2021~~, Atmos. Chem. Phys., 21(18), 14371–14384, https://doi.org/10.5194/acp-21-14371-2021, 2021.

Che, H., Gui, K., Xia, X., Wang, Y., Holben, B. N., Goloub, P., Cuevas-Agulló, E., Wang, H., Zheng, Y., Zhao, H., ~~&~~and Zhang, X~~. (2019).~~.: Large contribution of meteorological factors to inter-decadal changes in regional aerosol optical depth~~. *Atmospheric Chemistry and Physics, 19*(16), 10497–10523. https://doi.org/10.5194/acp-19-10497-2019~~, Atmos. Chem. Phys., 19(16), 10497–10523, https://doi.org/10.5194/acp-19-10497-2019, 2019

Collis, R. T. H. and Russell, P. B.: Lidar Measurement of ~~Particles~~particles and ~~Gases~~gases by ~~Elastic~~elastic backscattering and ~~Differential~~differential absorption, in: Laser Monitoring of the Atmosphere, edited by: Hinkley, E. D., Springer Verlag, Berlin, Germany, ~~1976~~71-151, https://doi.org/10.1007/3-540-07743-X_18, 2005.

~~Draxler, R. R., & Hess, G. D. (1998). An overview of the HYSPLIT_4 modelling system for trajectories, dispersion and deposition. *Australian Meteorological Magazine, 47*(4), 295–308.~~

Fadnavis, S., Chavan, P., Joshi, A., Sonbawne, S. M., Acharya, A., Devara, P. C. S., Rap, A., Ploeger, F., ~~&~~and Müller, R~~. (2022).~~.: Tropospheric warming over the northern Indian Ocean caused by South Asian anthropogenic aerosols: Possible impact on the upper troposphere and lower stratosphere~~. *Atmospheric Chemistry and Physics, 22*(11), 7179–7191. https://doi.org/10.5194/acp-22-7179-2022~~, Atmos. Chem. Phys., 22(11), 7179–7191, https://doi.org/10.5194/acp-22-7179-2022, 2022.

Fadnavis, S., Semeniuk, K., Pozzoli, L., Schultz, M. G., Ghude, S. D., Das, S., ~~&~~and Kakatkar, R~~.~~

~~(2013).~~.: Transport of aerosols into the UTLS and their impact on the ~~asian~~Asian monsoon region as seen in a global model simulation~~. *Atmospheric Chemistry and Physics*,~~, Atmos. Chem. Phys., 13(17), 8771–8786~~. https://doi.org/10.5194/acp-13-8771-2013~~, https://doi.org/10.5194/acp-13-8771-2013, 2013.

Fairlie, T. D., Liu, H., Vernier, J. P., Campuzano-Jost, P., Jimenez, J. L., Jo, D. S., Zhang, B., Natarajan, M., Avery, M. A., ~~&~~and Huey, G~~. (2020).~~.: Estimates of Regional Source Contributions to the Asian Tropopause Aerosol Layer Using a Chemical Transport Model~~.~~ ~~*Journal of Geophysical Research: Atmospheres*, *125*(4), 1–20. https://doi.org/10.1029/2019JD031506~~, J. Geophys. Res.-Atmos., 125(4), 1–20, https://doi.org/10.1029/2019JD031506, 2020.

Gadhavi, H~~., &~~. and Jayaraman, A~~. (2006).~~.: Airborne lidar study of the vertical distribution of aerosols over Hyderabad, an urban site in central India, and its implication for radiative forcing calculations~~. *Annales Geophysicae*, *24*(10), 2461–2470. https://doi.org/10.5194/angeo-24-2461-2006~~, *Ann. Geophys.*, 24, 2461–2470, https://doi.org/10.5194/angeo-24-2461-2006, 2006.

Gao, J., Huang, Y., Peng, Y., ~~&~~and Wright, J. S~~. (2023).~~.: Aerosol Effects on Clear-Sky Shortwave Heating in the Asian Monsoon Tropopause Layer~~. *Journal of Geophysical Research: Atmospheres*,~~, J. Geophys. Res.-Atmos., 128(4), 1–23~~. https://doi.org/10.1029/2022JD036956~~, https://doi.org/10.1029/2022JD036956, 2023.

Gupta, G., Ratnam, M. V., Madhavan, B. L., Prasad, P., ~~&~~and Narayanamurthy, C. S~~. (2021).~~.: Vertical and spatial distribution of elevated aerosol layers obtained using long-term ground-based and space-borne lidar observations~~. *Atmospheric Environment*, *246*(September 2020), 118172. https://doi.org/10.1016/j.atmosenv.2020.118172~~, Atmos. Environ., 246, 118172. https://doi.org/10.1016/j.atmosenv.2020.118172, 2021.

Hanumanthu, S., Vogel, B., Müller, R., Brunamonti, S., Fadnavis, S., Li, D., Ölsner, P., Naja, M., Singh, B. B., Kumar, K. R., Sonbawne, S., Jauhiainen, H., Vömel, H., Luo, B., Jorge, T., Wienhold, F. G., Dirkson, R., ~~&~~and Peter, T~~. (2020).~~.: Strong day-to-day variability of the Asian Tropopause Aerosol Layer (ATAL) in August 2016 at the Himalayan foothills~~.~~ ~~*Atmospheric Chemistry and Physics*, *20*(22), 14273–14302. https://doi.org/10.5194/acp-20-14273-2020~~, Atmos. Chem. Phys., 20(22), 14273–14302, https://doi.org/10.5194/acp-20-14273-2020, 2020.

He, Q., Ma, J., Zheng, X., Wang, Y., Wang, Y., Mu, H., Cheng, T., He, R., Huang, G., Liu, D., ~~&~~and Lelieveld, J~~. (2020).~~.: Formation and dissipation dynamics of the Asian tropopause aerosol layer~~. *Environmental Research Letters*,~~, Environ. Res. Letts., 16(1~~). https://doi.org/10.1088/1748-9326/abcd5d~~), https://doi.org/10.1088/1748-9326/abcd5d, 2020.

~~He, Q., Ma, J., Zheng, X., Yan, X., Vömel, H., Wienhold, F. G., Gao, W., Liu, D., Shi, G., &~~

~~Cheng, T. (2019). Observational evidence of particle hygroscopic growth in the upper troposphere–lower stratosphere (UTLS) over the Tibetan Plateau. *Atmospheric Chemistry and Physics*, *19*(13), 8399–8406. https://doi.org/10.5194/acp-19-8399-2019~~

Hess, M., Koepke, P., ~~&~~and Schult, I~~. (1998).~~.: Optical Properties of Aerosols and Clouds: The Software Package OPAC~~. *Bulletin of the American Meteorological Society*,~~, Bull. Am. Meteorol. Soc., 79(5), 831–844~~. https://doi.org/10.1175/1520-0477(1998)079<0831:OPOAAC>2.0.CO;2~~, https://doi.org/10.1175/1520-0477(1998)079<0831:OPOAAC>2.0.CO;2, 1998.

~~Höpfner, M., Ungermann, J., Borrmann, S., Wagner, R., Spang,~~Höpfner, M., Ungermann, J., Borrmann, S. et al.:~~R., Riese, M., Stiller, G., Appel, O., Batenburg, A. M., Bucci, S., Cairo, F., Dragoneas, A., Friedl-Vallon, F., Hünig, A., Johansson, S., Krasauskas, L., Legras, B., Leisner, T., Mahnke, C., … Wohltmann, I. (2019).~~ Ammonium nitrate particles formed in upper troposphere from ground ammonia sources during Asian monsoons~~. *Nature Geoscience*, *12*(8), 608–612. https://doi.org/10.1038/s41561-019-0385-8~~, Nat. Geosci., 12(8), 608–612, https://doi.org/10.1038/s41561-019-0385-8, 2019.

~~Huang, Y., Zhang, M., Xia, Y., Hu, Y., & Son, S. W. (2016). Is there a stratospheric radiative feedback in global warming simulations? *Climate Dynamics*, *46*(1–2), 177–186. https://doi.org/10.1007/s00382-015-2577-2~~

~~Kalluri, R. O. R., Gugamsetty, B., Kotalo, R. G., Thotli, L. R., Tandule, C. R., & Akkiraju, B. (2020). Long-term (2008–2017) analysis of atmospheric composite aerosol and black carbon radiative forcing over a semi-arid region in southern India: Model results and ground measurement. *Atmospheric Environment*, *240*(August), 117840. https://doi.org/10.1016/j.atmosenv.2020.117840~~

~~Kloss, C., Berthet, G., Sellitto, P.,~~ Junge, C. E. and Manson, J. E.: Stratospheric aerosol studies, *J. Geophys. Res.*, 66, 7, 2163–2182, https://doi.org/10.1029/JZ066i007p02163, 1961.

~~Ploeger, F., Taha, G., Tidiga, M., Eremenko, M., Bossolasco, A., Jégou, F., Renard, J. B., & Legras, B. (2021). Stratospheric aerosol layer perturbation caused by the 2019 Raikoke and Ulawun eruptions and their radiative forcing. *Atmospheric Chemistry and Physics*, *21*(1),~~

~~535–560. https://doi.org/10.5194/acp-21-535-2021~~

Komhyr, W. D., Barnes, R. A., Brothers, G. B., Lathrop, J. A., ~~&~~and Opperman, D. P~~. (1995).~~.: Electrochemical concentration cell ozonesonde performance evaluation during STOIC 1989~~.~~ ~~*Journal of Geophysical Research*, *100*~~, J. Geophys. Res., (D5), 9231–9244~~.~~ ~~https://doi.org/10.1029/94JD02175~~, https://doi.org/10.1029/94JD02175, 1995.

Kumar, A. H., ~~&~~and Ratnam, M. V~~. (2021).~~.: Variability in the UTLS chemical composition during different modes of the Asian Summer Monsoon Anti-cyclone~~. *Atmospheric Research*, *260*(May), 105700. https://doi.org/10.1016/j.atmosres.2021.105700~~, Atmos. Res., 260, 105700, https://doi.org/10.1016/j.atmosres.2021.105700, 2021.

Lau, W. K. M., Yuan, C., ~~&~~and Li, Z~~. (2018).~~.: Origin, Maintenance and Variability of the Asian Tropopause Aerosol Layer (ATAL): The Roles of Monsoon Dynamics~~. *Scientific Reports*, *8*(1), 1–14. https://doi.org/10.1038/s41598-018-22267-z~~, Sci. Rep., 8(1), 1–14, https://doi.org/10.1038/s41598-018-22267-z, 2018.

Lelieveld, J., Bourtsoukidis, E., Brühl, C., Fischer, H., Fuchs, H., Harder, H., Hofzumahaus, A., Holland, F., Marno, D., Neumaier, M., Pozzer, A., Schlager, H., Williams, J., Zahn, A., & Ziereis, H.: The South Asian monsoon—Pollution pump and purifier. *Science*, *361*(6399), 270–273. https://doi.org/10.1126/science.aar2501, 2018.

Liou, K. N~~. (2002).~~.: An Introduction to Atmospheric Radiation, 2nd Edition, Academic Press~~:~~, Cambridge, MA, USA, 1053 pp., ISBN 9780123958259, 2002.

~~Li, Q., Jiang, J. H., Wu, D. L., Read, W. G., Livesey, N. J., Waters, J. W., Zhang, Y., Wang, B., Filipiak, M. J., Davis, C. P., Turquety, S., Wu, S., Park, R. J., Yantosca, R. M., & Jacob, D. J. (2005). Convective outflow of South Asian pollution: A global CTM simulation compared with EOS MLS observations. *Geophysical Research Letters*, *32*(14), 1–4. https://doi.org/10.1029/2005GL022762~~

Ma, J., Brühl, C., He, Q., Steil, B., Karydis, V. A., Klingmüller, K., Tost, H., Chen, B., Jin, Y., Liu, N., Xu, X., Yan, P., Zhou, X., Abdelrahman, K., Pozzer, A., ~~&~~and Lelieveld, J~~. (2019).~~.: Modeling the aerosol chemical composition of the tropopause over the Tibetan Plateau during the Asian summer monsoon~~. *Atmospheric Chemistry and Physics*, *19*(17), 11587–11612. https://doi.org/10.5194/acp-19-11587-2019~~, Atmos. Chem. Phys., 19(17), 11587–11612, https://doi.org/10.5194/acp-19-11587-2019, 2019.

Madhavan, B. L., Krishnaveni, A. S., Ratnam, M. V., ~~& Ravikiran~~and Ravi Kiran, V~~. (2021).~~.: Climatological aspects of size-resolved column aerosol optical properties over a rural site in the southern peninsular India~~. *Atmospheric Research*, *249*(September 2020), 105345. https://doi.org/10.1016/j.atmosres.2020.105345~~, Atmos. Res., 249, 105345, https://doi.org/10.1016/j.atmosres.2020.105345, 2021.

Miloshevich, L. M., Vömel, H., Whiteman, D. N., Lesht, B. M., Schmidlin, F. J., and Russo, F.: Absolute accuracy of water vapor measurements from six operational radiosonde types launched during AWEX-G, and implications for AIRS validation, *J. Geophys. Res.*, **111**, D09S10, https://doi.org/10.1029/2005JD006083, 2006.

~~Mahnke, C., Weigel, R., Cairo, F., Vernier, J. P., Afchine, A., Krämer, M., Mitev, V., Matthey, R., Viciani, S., D'Amato, F., Ploeger, F., Deshler, T., & Borrmann, S. (2021). The Asian tropopause aerosol layer within the 2017 monsoon anticyclone: Microphysical properties derived from aircraft-borne in situ measurements. *Atmospheric Chemistry and Physics*, *21*(19), 15259–15282. https://doi.org/10.5194/acp-21-15259-2021~~

Murari, V., Kumar, M., Mhawish, A., Barman, S. C., ~~&~~and Banerjee, T~~. (2017).~~.: Airborne particulate in Varanasi over middle Indo-Gangetic Plain: variation in particulate types and meteorological influences~~. *Environmental Monitoring and Assessment*, *189*(4). https://doi.org/10.1007/s10661-017-5859-9~~, Environ. Monit. Assess., 189(4), https://doi.org/10.1007/s10661-017-5859-9, 2017.

Neely, R. R., Yu, P., Rosenlof, K. H., Toon, O. B., Daniel, J. S., Solomon, S., ~~&~~and Miller, H. L~~. (2014).~~.: The contribution of anthropogenic SO2 emissions to the Asian tropopause aerosol layer~~. *Journal of Geophysical Research*,~~, J. Geophys. Res., 119(3), 1571–1579. ~~https://doi.org/10.1002/2013JD020578~~https://doi.org/10.1002/2013JD020578, 2014.

~~Niranjan, K., Madhavan, B. L., & Sreekanth, V. (2007). Micro pulse lidar observation of high altitude aerosol layers at Visakhapatnam located on the east coast of India. *Geophysical Research Letters*, *34*(3), 5–9. https://doi.org/10.1029/2006GL028199~~

Park, M., Randel, W. J., Gettelman, A., Massie, S. T., ~~&~~and Jiang, J. H~~. (2007).~~.: Transport above the Asian summer monsoon anticyclone inferred from Aura Microwave Limb Sounder tracers~~. *Journal of Geophysical Research Atmospheres*, *112*(16), 1–13. https://doi.org/10.1029/2006JD008294~~, J. Geophys. Res.-Atmos., 112(16), 1–13, https://doi.org/10.1029/2006JD008294, 2007.

Pawar, G.~~-~~V., Devara, P.~~-~~C.~~-~~S., ~~&~~and Aher, G.~~-~~R~~. (2015).~~.: Identification of aerosol types over an urban site based on air-mass trajectory classification~~. *Atmospheric Research*,~~, Atmos. Res., 164~~–~~-165, 142~~–~~-155. ~~https://doi.org/10.1016/j.atmosres.2015.04.022~~https://doi.org/10.106/j.atmosres.2015.04.022, 2015.

Randel, W. J., ~~&~~and Park, M~~. (2006).~~.: Deep convective influence on the Asian summer monsoon anticyclone and associated tracer variability observed with Atmospheric Infrared Sounder (AIRS~~). *Journal of Geophysical Research Atmospheres*, *111*(12), 1–13. https://doi.org/10.1029/2005JD006490~~), J. Geophys. Res.-Atmos., 111(12), 1–13, https://doi.org/10.1029/2005JD006490, 2006.

~~Ravi Kiran, V., Ratnam, M. V., Fujiwara, M., Russchenberg, H., Wienhold, F. G., Madhavan, B. L., Raman, M. R., Nandan, R., Akhil Raj, S. T., Kumar, A. H., & Babu, S. R. (2022). Balloon-borne aerosol-cloud interaction studies (BACIS): field campaigns to understand and quantify aerosol effects on clouds. *Atmospheric Measurement Techniques*, *15*(16), 4709–4734. https://doi.org/10.5194/amt-15-4709-2022~~

~~Ratnam, M. V., Prasad, P., Roja Raman, M., Ravikiran, V., Bhaskara Rao, S. V., Krishna Murthy, B. V., & Jayaraman, A. (2018). Role of dynamics on the formation and maintenance of the elevated aerosol layer during monsoon season over south-east peninsular India. *Atmospheric Environment*, *188*(June), 43–49. https://doi.org/10.1016/j.atmosenv.2018.06.023~~

Ratnam, M. V., Raj, S. T. A., Madhavan, B. L., Vernier, J. P., Kiran, V. R., Jain, C. D., Basha, G., Nagendra, N., Kumar, B. S., Pandit, A. K., Murthy, B. V. K., & Jayaraman, A~~. (2020).~~.: Vertically resolved black carbon measurements and associated heating rates obtained using in situ balloon platform~~. *Atmospheric Environment*, *232* (January). https://doi.org/10.1016/j.atmosenv.2020.117541~~, Atmos. Environ., 232, https://doi.org/10.1016/j.atmosenv.2020.117541, 2020.

Ratnam, M.V, Sunilkumar, S. V., Parameswaran, K., Krishna Murthy, B. V., Ramkumar, G., Rajeev, K., Basha, G., Ravindra Babu, S., Muhsin, M., Kumar Mishra, M., Hemanth Kumar, A., Akhil Raj, S. T., ~~&~~and Pramitha, M~~. (2014).~~.: Tropical tropopause dynamics (TTD) campaigns over Indian region: An overview~~. *Journal of Atmospheric and Solar-Terrestrial Physics*,~~, J. Atmos. Sol.-Terr. Phys., 121(PB), 229–239~~. https://doi.org/10.1016/j.jastp.2014.05.007~~, https://doi.org/10.1016/j.jastp.2014.05.007, 2014.

Ricchiazzi, P., Yang, S., Gautier, C., and Sowle, D.: SBDART: A research and teaching software tool for plane-parallel radiative transfer in the Earth's atmosphere, *Bull. Am. Meteorol. Soc.*, 79, 2101–2114, 1998.

Santhosh, V. N., Madhavan, B. L., ~~Robrecht, S., Vogel, B., Grooß, J. U., Rosenlof, K., Thornberry, T., Rollins, A., Krämer, M., Christensen,~~and Venkat Ratnam, M.: Quantifying shortwave radiative forcing and heating rates of UTLS aerosols in the Asian summer monsoon anticyclone region, *J. Quant. Spectrosc. Ra.*, 339, 109430, https://doi.org/10.1016/j.jqsrt.2025.109430, 2025.

~~L., & Müller, R. (2019). Mechanism of ozone loss under enhanced water vapour conditions in the mid-latitude lower stratosphere in summer. *Atmospheric Chemistry and Physics*, *19*(9), 5805–5833. https://doi.org/10.5194/acp-19-5805-2019~~

Santhosh, V. N., Madhavan, B. L., Ratnam, M. V., Naik, D. N., ~~&~~and Sellitto, P~~. (2024).~~.: Assessing biases in atmospheric parameters for radiative effects estimation in tropical regions~~. *Journal of Quantitative Spectroscopy and Radiative Transfer*,~~, J. Quant. Spectrosc. Radiat. Transf., 314~~(August 2023),~~, 108858~~.~~, ~~https://doi.org/10.1016/j.jqsrt.2023.108858~~https://doi.org/10.1016/j.jqsrt.2023.108858, 2024a.

Santhosh, V. N., Madhavan, B. L., Ratnam, M. V., ~~&~~and Naik, D. N~~. (2024).~~.: Influence of columnar versus vertical distribution of aerosol properties on the modulation of shortwave radiative effects~~. *Journal of Quantitative Spectroscopy and Radiative Transfer*, *329*(March), 109179. https://doi.org/10.1016/j.jqsrt.2024.109179~~, J. Quant. Spectrosc. Radiat. Transf., 329, 109179, https://doi.org/10.1016/j.jqsrt.2024.109179, 2024b.

~~Sarangi, C., Tripathi, S. N., Mishra, A. K., Goel, A., & Welton, E. J. (2016). Elevated aerosol layers and their radiative impact over Kanpur during monsoon onset period. *Journal of Geophysical Research*, *121*(13), 7936–7957. https://doi.org/10.1002/2015JD024711~~

~~Schmidt, A., Mills, M. J., Ghan, S., Gregory, J. M., Allan, R. P., Andrews, T., Bardeen, C. G., Conley, A., Forster, P. M., Gettelman, A., Portmann, R. W., Solomon, S., & Toon, O. B. (2018). Volcanic Radiative Forcing From 1979 to 2015. *Journal of Geophysical Research: Atmospheres*, *123*(22), 12,491–12,508. https://doi.org/10.1029/2018JD028776~~

Sinha, P. R., Dumka, U. C., Manchanda, R. K., Kaskaoutis, D. G., Sreenivasan, S., Krishna Moorthy, K., ~~&~~and Suresh Babu, S~~. (2013).~~.: Contrasting aerosol characteristics and radiative forcing over Hyderabad, India due to seasonal mesoscale and synoptic-scale processes, Q. J. R. ~~. *Quarterly Journal of the Royal Meteorological Society*,~~Meteorol. Soc., 139(671), 434–450. ~~https://doi.org/10.1002/qj.1963~~https://doi.org/10.1002/qj.1963, 2013.

~~Sinha, P. R., Kaskaoutis, D. G., Manchanda, R. K., & Sreenivasan, S. (2012). Characteristics of aerosols over Hyderabad in southern Peninsular India: Synergy in the classification techniques. *Annales Geophysicae*, *30*(9), 1393–1410. https://doi.org/10.5194/angeo-30-1393-2012~~

Solomon, S., Daniel, J. S., Neely, R. R., Vernier, J. P., Dutton, E. G., ~~&~~and Thomason, L. W~~.~~ ~~(2011).~~.: The persistently variable "background" stratospheric aerosol layer and global climate change~~.~~, Science, 333(6044), 866–870~~. https://doi.org/10.1126/science.1206027~~, https://doi.org/10.1126/science.1206027, 2011.

Stamnes, K., Tsay, S.-C., Wiscombe, W., ~~&~~and Jayaweera, K~~. (1988).~~.: Numerically stable algorithm for discrete-ordinate-method radiative transfer in multiple scattering and emitting layered media~~. *Applied Optics*, *27*(12), 2502. https://doi.org/10.1364/ao.27.002502~~, App. Opt., 27(12), 2502, https://doi.org/10.1364/ao.27.002502, 1988.

Stein, A. F., Draxler, R. R., Rolph, G. D., Stunder, B. J. B., Cohen, M. D., ~~&~~and Ngan, F~~. (2015). Noaa's~~.: NOAA's hysplit atmospheric transport and dispersion modeling system~~. *Bulletin of the American Meteorological Society*,~~, Bull. Amer. Meteor. Soc., 96(12), 2059–2077~~. https://doi.org/10.1175/BAMS-D-14-00110.1~~, https://doi.org/10.1175/BAMS-D-14-00110.1, 2015.

~~Subba, T., Gogoi, M. M., Moorthy, K. K., Bhuyan, P. K., Pathak, B., Guha, A., Srivastava, M. K., Vyas, B. M., Singh, K., Krishnan, J., Lakshmi Kumar, T. V., & Babu, S. S. (2022). New estimates of aerosol radiative effects over India from surface and satellite observations. *Atmospheric Research*, *276*(December 2021), 106254. https://doi.org/10.1016/j.atmosres.2022.106254~~

Thomason, L. W., ~~&~~and Vernier, J. P~~. (2013).~~.: Improved SAGE II cloud/aerosol categorization and observations of the Asian tropopause aerosol layer: 1989-2005~~. *Atmospheric Chemistry and Physics*, *13*(9), 4605–4616. https://doi.org/10.5194/acp-13-4605-2013~~, Atmos. Chem. Phys., 13(9), 4605–4616, https://doi.org/10.5194/acp-13-4605-2013, 2013.

Tiwari, S., ~~&~~and Singh, A. K~~. (2013).~~.: Variability of Aerosol parameters derived from ground and satellite measurements over Varanasi located in the Indo-Gangetic Basin~~.~~, Aerosol ~~*and*~~ Air ~~*Quality Research*,~~Qual. Res., 13(2), 627–638. ~~https://doi.org/10.4209/aaqr.2012.06.0162~~https://doi.org/10.4209/aaqr.2012.06.0162, 2013.

~~Vaishya, A., Nair, S., Babu, S., Jayachandran, V., & Gogoi, M. M. (2018). *Large contrast in the vertical distribution of aerosol optical properties and radiative effects across the Indo-Gangetic Plain during the SWAAMI – RAWEX campaign*. 17669–17685.~~

Vernier, H., Rastogi, N., Liu, H., Pandit, A. K., Bedka, K., Patel, A., Ratnam, M. V., Kumar, B. S., Zhang, B., Gadhavi, H., Wienhold, F., Berthet, G., ~~&~~and Vernier, J. P~~. (2022).~~.: Exploring the inorganic composition of the Asian Tropopause Aerosol Layer using medium-duration balloon flights~~. *Atmospheric Chemistry and Physics*,~~, Atmos. Chem. Phys., 22(18), 12675–12694. ~~https://doi.org/10.5194/acp-22-12675-2022~~https://doi.org/10.5194/acp-22-12675-2022, 2022.

Vernier, J. P., Fairlie, T. D., ~~Deshler, T., Venkat Ratnam, M., Gadhavi, H., Kumar, B. S., Natarajan, M., Pandit, A. K., Akhil Raj, S. T., Hemanth Kumar, A., Jayaraman, A., Singh, A. K., Rastogi,~~ et al.:~~N., Sinha, P. R., Kumar, S., Tiwari, S., Wegner, T., Baker, N., Vignelles, D., … Renard, J. B. (2018).~~ BATAL: The balloon measurement campaigns of the Asian tropopause aerosol layer~~. *Bulletin of the American Meteorological Society*,~~, Bull. Am. Meteor. Soc., 99(5), 955–973~~. https://doi.org/10.1175/BAMS-D-17-0014.1,~~ https://doi.org/10.1175/BAMS-D-17-0014.1, 2018.

Vernier, J. P., Thomason, L. W., ~~&~~and Kar, J~~. (2011).~~.: CALIPSO detection of an Asian tropopause aerosol layer~~. *Geophysical Research Letters*,~~, Geophys. Res. Lett., 38(7), 1–6~~.~~, ~~https://doi.org/10.1029/2010GL046614~~https://doi.org/10.1029/2010GL046614, 2011.

Vernier, J.-P., T. D. Fairlie, M. Natarajan, F. G. Wienhold, J. Bian, B. G. Martinsson, S. Crumeyrolle, L. W. Thomason, and K. M. Bedka~~ (2015),~~: Increase in upper tropospheric and lower stratospheric aerosol levels and its potential connection with Asian pollution, J. Geophys. Res~~. –~~.-Atmos., 120, 1608–1619, https://doi~~:~~.org/10.1002/2014JD022372, 2015.

Vogel, B., Volk, C. M., Wintel, J., Lauther, V., Clemens, J., Grooß, J.-U., Günther, G., Hoffmann, L., Laube, J. C., Müller, R., Ploeger, F., & Stroh, F.: Evaluation of vertical transport in ERA5 and ERA-Interim reanalysis using high-altitude aircraft measurements in the Asian summer monsoon 2017. *Atmospheric Chemistry and Physics*, *24*(1), 317–343. https://doi.org/10.5194/acp-24-317-2024, 2024.

Von Hobe, M., Ploeger, F., Konopka, P., Kloss, C., Ulanowski, A., Yushkov, V., Ravegnani, F., Volk, C. M., Pan, L. L., Honomichl, S. B., Tilmes, S., Kinnison, D. E., Garcia, R. R., & Wright, J. S.: Upward transport into and within the Asian monsoon anticyclone as inferred from StratoClim trace gas observations. *Atmospheric Chemistry and Physics*, *21*(2), 1267–

1285. https://doi.org/10.5194/acp-21-1267-2021, 2021.

Xu, H., Guo, J., Tong, B., Zhang, J., Chen, T., Guo, X., Zhang, J., ~~&~~and Chen, W~~. (2023).~~.: Characterizing the near-global cloud vertical structures over land using high-resolution radiosonde measurements~~. *Atmospheric Chemistry and Physics*,~~, Atmos. Chem. Phys., 23(23), 15011–15038. ~~https://doi.org/10.5194/acp-23-15011-2023~~https://doi.org/10.5194/acp-23-15011-2023, 2023.

Yu, P., Lian, S., Zhu, Y., Toon, O. B., Höpfner, M., ~~&~~and Borrmann, S~~. (2022).~~.: Abundant Nitrate and Nitric Acid Aerosol in the Upper Troposphere and Lower Stratosphere~~. *Geophysical Research Letters*,~~, Geophys. Res. Lett., 49(18~~). https://doi.org/10.1029/2022GL100258~~), https://doi.org/10.1029/2022GL100258, 2022.

Yu, P., Rosenlof, K. H., Liu, S., Telg, H., Thornberry, T. D., Rollins, A. W., Portmann, R. W., Bai, Z., Ray, E. A., Duan, Y., Pan, L. L., Toon, O. B., Bian, J., & Gao, R.-S.: Efficient transport of tropospheric aerosol into the stratosphere via the Asian summer monsoon anticyclone. *Proceedings of the National Academy of Sciences*, *114*(27), 6972–6977. https://doi.org/10.1073/pnas.1701170114, 2017.

Yu, P., Toon, O. B., Neely, R. R., Martinsson, B. G., ~~&~~and Brenninkmeijer, C. A. M~~. (2015).~~.: Composition and physical properties of the Asian Tropopause Aerosol Layer and the North American Tropospheric Aerosol Layer~~. *Geophysical Research Letters*, *42*(7), 2540–2546. https://doi.org/10.1002/2015GL063181~~, Geophys. Res. Lett., 42(7), 2540–2546. https://doi.org/10.1002/2015GL063181, 2015.

Zhang, H., Shen, Z., Wei, X., Zhang, M., ~~&~~and Li, Z~~. (2012).~~.: Comparison of optical properties of nitrate and sulfate aerosol and the direct radiative forcing due to nitrate in China~~.~~ ~~*Atmospheric Research*,~~, Atmos. Res., 113, 113–125, https://doi.org/10.1016/j.atmosres.2012.04.020, 2012.

Zhu, Y., Yu, P., Wang, X., Bardeen, C., Borrmann, S., Höpfner, M., Mahnke, C., Weigel, R., Krämer, M., Deshler, T., Bian, J., Bai, Z., Vernier, H., Portmann, R. W., Rosenlof, K. H., Kloss, C., Pan, L. L., ~~. https://doi.org/10.1016/j.atmosres.2012.04.020~~Smith, W., Honomichl, S., … Toon, O. B.: Evaluating the Importance of Nitrate-Containing Aerosols for the Asian Tropopause Aerosol Layer. *Journal of Geophysical Research: Atmospheres*, *129*(19), e2024JD041283. https://doi.org/10.1029/2024JD041283, 2024.